

UNIVERSITÀ DEGLI STUDI DI PADOVA
DIPARTIMENTO DI SCIENZE CHIMICHE
DIPARTIMENTO DI FISICA
CORSO DI LAUREA MAGISTRALE IN SCIENZA DEI
MATERIALI

TESI DI LAUREA MAGISTRALE
DESIGN AND FABRICATION OF BIFUNCTIONAL
METALENSES

Relatore: **Filippo Romanato**

Correlatore: **Andrea Vogliardi**

LAUREANDO: **Daniele Bonaldo**

Anno accademico: 2021-2022

Contents

Acknowledgments	1
Introduction	2
1 Theoretical framework	5
1.1 Propagation of light	5
1.2 Metalenses	8
1.3 Definition of the to-be fabricated metalenses	11
2 Design of metalenses	13
2.1 Design of meta-atoms	13
2.1.1 Setting of FEM simulations	13
2.1.2 Results of simulations	15
2.2 Mapping of meta-atoms	21
2.3 Simulation of the devices	24
2.3.1 Fourier optics	24
2.3.2 Simulation algorithm and results	25
3 Principles of lithography	29
3.1 Introduction	29
3.2 Resists	30
3.3 Spin coating	32
3.4 Exposure	33
3.4.1 Electron Beam Lithographer	34
3.4.2 Electron collisions and proximity effect	36
3.5 Development	39
3.6 Hard mask deposition and lift-off	39
3.7 Reactive Ion Etching	40
4 Fabrication of metalenses	45
4.1 Spin coating	46

4.2	Exposure and development	47
4.2.1	PECless patterns	47
4.2.2	Proximity effect correction	50
4.2.3	PEC patterns	52
4.3	Hard mask deposition and lift-off	53
4.4	ICP-RIE	55
4.5	Summary of processes and parameters	56
5	Optical characterization	59
5.1	Experimental set-up	59
5.2	Results	60
	Conclusions	63

Acknowledgments

I would like to thank my supervisor, professor Filippo Romanato, for helping me laying out this thesis and for guiding me through it. A special thank to Simone dal Zilio and Andrea Vogliardi, who dedicated much of their time to teach me and, more often than I would like to admit, to actually execute many needed processes, since a newbie as I was couldn't perform them in the dedicated timeframe. I would like to thank Gianluca Ruffato, Nicola Argiolas, Antonella Glisenti and Omar Veneziani for their technical and administrative support. Last but certainly not the least, a special thank to my family and my friends for providing the social support that everyone needs to retain motivation and happiness.

This work completes a journey which began five years ago in the University of Padova, at that time I wasn't aware of the sheer amount of passion and ingenuity that would had stemmed from it.

*This present moment
used to be
the unimaginable future*
Stewart Brand

Introduction

Optics is still mainly relying on systems made of mirrors and lenses, for which high quality comes at high costs due to old hardly-scalable production processes. Moreover, they suffer from aberrations, which can be compensated only through multiple optical elements, increasing costs, bulkiness and weight. The call for more compact devices has led to development of metasurfaces (or metalenses): arrays of sub-wavelength-spaced optical scatterers, called meta-atoms, which locally apply a phase shift to incident light. By tailoring sizes and shapes of such nanostructures across the surface, any phase delay profile can be encoded to the device. Against diffraction-based optics, metasurfaces display higher diffraction efficiencies and easier fabrication, respectively due to the smaller spacing and fixed height of their building blocks. Metasurfaces are therefore gaining wide attention as potential substitutes of older technologies; all-dielectric devices, in particular, are interesting because of their higher efficiencies compared to plasmonic ones.

But there's more. Optics with flexible phase profiles unlocks new features in light beams, thanks to the complete control over the spatial distribution of their wavefront. In fact, the wavefront of light beams can be engineered to obtain a precise shape through the local modification of the phase of the electromagnetic wave. This process is known as light structuring and can be realized through the use of dedicated optics. The most popular light structuring feature is the generation of helicoidal wavefronts, with the presence of the so-called vortex singularity, which provide light with orbital angular momentum (OAM). OAM light has potential applications in microscopy^[19], particle trapping^[9] and communication^[31]. Generation and handling of OAM light can be achieved through the use of metalenses.

A particular type of metalenses are defined bifunctional, they can apply completely different phase profiles to orthogonal spin states, such as RCP and LCP polarizations, thanks to ad-hoc tailoring of meta-atoms' birefringence^[30]. Multifunctionality reduces the number of devices required for a given application, leading to more compact optical systems. Moreover, coupled with a polarization modulator, the two phase profiles can be switched back and forth, giving a dynamic optical system. Its switching frequency would be limited only by the modulator, which can reach the GHz range^[4]. High frequency switching is fundamental for communication, therefore bifunctional metalenses may enable OAM

light to be used in such field.

Fibre communication works at mid-IR frequencies; to our knowledge, there is only one study regarding mid-IR bifunctional metalenses, but it relies on reflection by plasmonic meta-atoms, which is inefficient and may be inconvenient for some optical architectures^[7]. The aim of this thesis has been the design, fabrication and characterization of all-dielectric, transmission-based, bifunctional metalenses working at 1310 nm; their fabrication had to be performed through standard lithographic techniques, which can be scaled up to industrial levels. These devices have a potential not only for communication purposes, but also for microscopy applications and particle trapping.

§ 1 covers the theoretical framework of OAM beams and metalenses. The design process was carried out through the meta-atoms simulation with finite element method analysis, described in § 2. Nanofabrication of the devices, performed through standard lithographic techniques, is covered in § 3 and § 4. Finally, their behaviour was characterized by laser illumination and the quality of the intensity patterns has been evaluated in § 5.

Chapter 1

Theoretical framework

1.1 Propagation of light

The description of optical devices requires an appropriate description of light. It can be described in more than one way, the choice depends on the phenomena involved. For example, the geometric description, which considers light as a beam of rays, is enough when dealing with lenses and mirrors. It can also give some insights about total internal reflection, the basic phenomenon behind propagation in waveguides, but the electromagnetic description of light is much more appropriate for our tasks, since they involve propagation along nanostructured dielectric interfaces and OAM beams. Within electromagnetic optics, light is an electromagnetic field which satisfy the source-free and current-free Maxwell equations:

$$\nabla \times H = \frac{\partial D}{\partial t} \quad (1.1)$$

$$\nabla \times E = -\frac{\partial B}{\partial t} \quad (1.2)$$

$$\nabla \cdot D = 0 \quad (1.3)$$

$$\nabla \cdot B = 0 \quad (1.4)$$

where $H = H(\mathbf{r}, t)$ and $E = E(\mathbf{r}, t)$ are respectively the magnetic vector field and the electric vector field; as for $D = D(\mathbf{r}, t)$ and $B = B(\mathbf{r}, t)$, the electric and magnetic displacement field, they are related to E and H in linear and homogeneous media through:

$$D = \epsilon E \quad (1.5)$$

$$B = \mu H \quad (1.6)$$

where ϵ, μ are the electric permittivity and the magnetic permeability of the medium. By

combining the Maxwell equations, the wave equation can be obtained:

$$\nabla^2 U - \frac{1}{c^2} \frac{\partial^2 U}{\partial t^2} = 0 \quad (1.7)$$

where U is either E or H , and $c = (\epsilon\mu)^{-\frac{1}{2}}$ is the speed of light in the medium. For a monochromatic wave with a given angular frequency ω and a complex amplitude $u(\mathbf{r})$:

$$U(\mathbf{r}, t) = U(\mathbf{r}) \exp(j\omega t) \quad (1.8)$$

the Helmholtz equation can be obtained from Equation 1.7 for $U(\mathbf{r})$:

$$\nabla^2 U + k^2 U = 0, \quad k = \frac{\omega}{c} = \text{wavenumber} \quad (1.9)$$

The simplest solution to the Helmholtz equation is the plane wave, which has a complex amplitude:

$$U(\mathbf{r}) = A \exp(-j\mathbf{k} \cdot \mathbf{r}) \quad (1.10)$$

Under the paraxial approximation $x^2 + y^2 \ll z^2$, which implies that we are examining a narrow beam propagating in the z direction, and by allowing the complex envelope to vary in space $A = A(\mathbf{r})$, we obtain the so-called paraxial wave:

$$U(\mathbf{r}) = A(\mathbf{r}) \exp(-jkz) \quad (1.11)$$

where the dependence on x and y is now being included in $A(\mathbf{r})$. The paraxial wave well describes light propagating along one direction without many assumption about its intensity profile. This generalization of the plane wave must satisfy Equation 1.9, from which we finally get the paraxial Helmholtz equation:

$$\nabla_T^2 A - j2k \frac{\partial A}{\partial z} = 0, \quad \nabla_T^2 = \frac{\partial^2}{\partial x^2} + \frac{\partial^2}{\partial y^2} \quad (1.12)$$

The simplest and most famous solution yields the Gaussian beam, whose envelope has a gaussian cross-section:

$$A(\mathbf{r}) = \frac{A_1}{q(z)} \exp\left(-jk \frac{\rho^2}{2q(z)}\right), \quad \rho^2 = x^2 + y^2, \quad q(z) = z + jz_0 \quad (1.13)$$

where z_0 is the Rayleigh range. The paraxial Helmholtz equation actually admits infinite solutions, a complete set of them is given by the Laguerre-Gaussian beams LG_{lm} . LG modes' intensity displays cylindrical symmetry, so cylindrical coordinates (ρ, ϕ, z) are

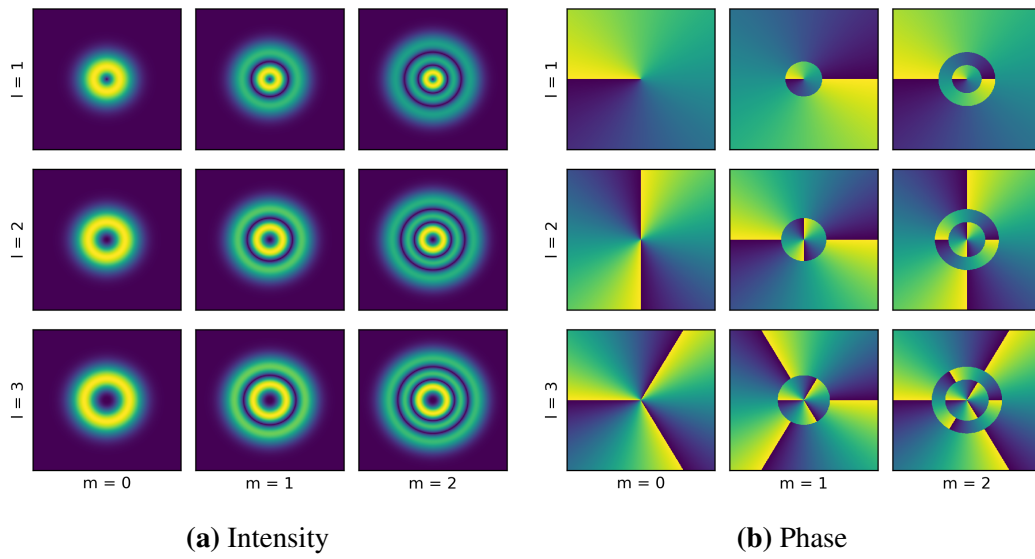


Figure 1.1: Intensity and phase profiles of the first Laguerre-Gaussian modes, calculated at $z = 0$

used for their representation, which reads:

$$U_{l,m}(\rho, \phi, z) = A_{l,m} \left[\frac{W_0}{W(z)} \right] \left(\frac{\rho}{W(z)} \right)^l \mathbb{L}_m^l \left(\frac{2\rho^2}{W^2(z)} \right) \exp \left(-\frac{\rho^2}{W^2(z)} \right) \quad (1.14)$$

$$\times \exp \left(-jkz - jk \frac{\rho^2}{2R(z)} \pm jl\phi + j(l+2m+1)\zeta(z) \right) \quad (1.15)$$

where:

$$\mathbb{L}_m^l(x) = (m+l)! \sum_{i=0}^m \frac{(-x)^i}{[i!(m-i)!(l+i)!]} \quad (\text{Generalized Laguerre Polynomials}) \quad (1.16)$$

$$W(z) = W_0 \sqrt{1 + \left(\frac{z}{z_0} \right)^2} \quad (1.17)$$

$$R(z) = z \left[1 + \left(\frac{z_0}{z} \right)^2 \right] \quad (1.18)$$

$$\zeta(z) = \tan^{-1} \frac{z}{z_0} \quad (1.19)$$

For $l, m = 0$ we retain the Gaussian beam, while for $l \neq 0$ the intensity at beam centre is zero and for $m > 0$ it takes the shape of multiple rings. Intensity and phase profiles of some LG modes are depicted in Fig. 1.1.

A peculiar property of such beams is the wavefront, which is an helical surface whose period and handedness depends on the modulus and sign of l , there are then m annular phase discontinuities corresponding to the intensity higher-order rings. Modes having a

helical wavefront carry orbital angular momentum (OAM) and they are often referred as OAM modes. It is not to be mistaken for the spin angular momentum (SAM), which is related to non-linear polarization, although they both counts as angular momenta and their sum, similarly to electrons, represents the total (internal) angular momentum of light. Their application is subject of research, involving optical tweezing, microscopy and communication, both in classical and quantum regimes^[6].

Generation of OAM light can be performed in many ways. The basic concept is to apply a phase-delay profile, such as those shown in Fig. 1.1b, to an incident plane-wave, the transmitted beam should be the corresponding LG mode. For example, a Spiral Phase Plates (SPP) is a dielectric layer with a helical optical-path length $k_0 n t(r, \theta) = l\theta$, generating LG_l^0 modes. Other solutions involve Spatial Light Modulators, mode conversion from Hermite-Gaussian beams and q-plates^[22]. Q-plates also exhibit an helical optical-path length, but the helicity is given by a space-varying refractive index $k_0 n(r, \theta) t = l\theta$, which is obtained either from liquid crystals or sub-wavelength gratings. The latter, known also as metalenses, attracted many researchers because of their greater flexibility in phase modulation, compatibility with semiconductor technologies, easy miniaturization and high efficiencies.

1.2 Metalenses

Propagation of light through linear dielectric materials is mostly described by the refractive index. In common human experience, objects have a characteristic size much greater than the wavelengths in the visible spectrum of light, therefore refractive indexes are univocally associated to homogeneous materials. Metalenses, instead, are characterized by sub-wavelength-sized nanostructures, the so-called meta-atoms; their effective local refractive index is between that of the air and of the solid material. By changing the size and shape of the meta-atom, we can finely tune the local refractive index and thus the transmission properties (Phase delay and transmittance). Any phase profile can be encoded in a metalens, therefore it represents a flexible mean of applying arbitrarily complex transformations to an incoming beam.

Conceptually, the easiest way to tune the optical properties of a nanostructure is by changing its size: since solids have a greater refractive index than air, the greater the size and the higher the effective refractive index. It is possible then to create a surface with a given phase-delay profile by fabricating an array of nanopillars with space-varying sizes, as depicted in Fig. 1.2. These kinds of metalenses exploit the so-called dynamic phase, which does not depends on polarization of the incoming beam.

There's another way of modulating the effective refractive index, that exploits circularly polarized light and birefringent meta-atoms. When circularly polarized light impinges on

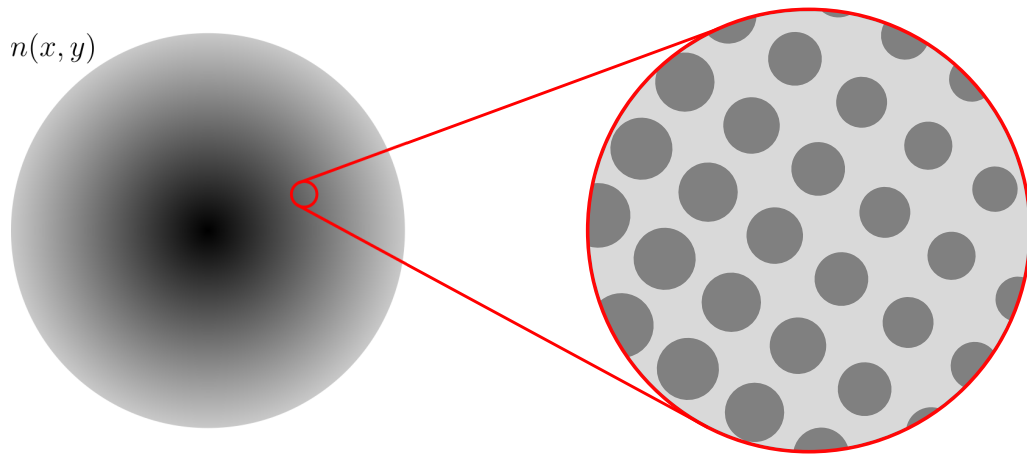


Figure 1.2: A space-varying $n(x, y)$ originating from an array of nanostructures with space-varying size.

an anisotropic medium, two distinct contributions to the phase delay arise: dynamic phase and geometric phase. It can be demonstrated through Jones' algebra; the impinging beam J_i and the anisotropic medium transformation T_0 can be represented as:

$$J_i = \begin{pmatrix} 1 \\ \pm i \end{pmatrix} \quad T_0 = \begin{pmatrix} e^{i\delta_x} & 0 \\ 0 & e^{i\delta_y} \end{pmatrix} = e^{i\frac{\delta_x+\delta_y}{2}} \begin{pmatrix} e^{-\delta/2} & 0 \\ 0 & e^{i\delta/2} \end{pmatrix} \quad \delta = \delta_y - \delta_x \quad (1.20)$$

where δ_x and δ_y are the phase delays for x and y polarized light in the anisotropic region. Now, if we apply a rotation θ of the medium around the propagation axis, the Jones matrix must be transformed through a change of basis:

$$R_\theta = \begin{pmatrix} \cos \theta & -\sin \theta \\ \sin \theta & \cos \theta \end{pmatrix} \quad (1.21)$$

$$T_\theta = R_\theta T_0 R_\theta^{-1} = e^{i\frac{\delta_x+\delta_y}{2}} \begin{pmatrix} e^{-\delta/2} \cos^2 \theta + e^{i\delta/2} \sin^2 \theta & -i \sin(2\theta) \sin(2\delta) \\ -i \sin(2\theta) \sin(2\delta) & e^{\delta/2} \cos^2 \theta + e^{-i\delta/2} \sin^2 \theta \end{pmatrix} \quad (1.22)$$

The resulting beam is given by:

$$T_\theta J_i = e^{i\frac{\delta_x+\delta_y}{2}} \cos \frac{\delta}{2} \begin{pmatrix} 1 \\ \pm i \end{pmatrix} - i e^{i\frac{\delta_x+\delta_y}{2}} \sin \frac{\delta}{2} e^{\mp 2i\theta} \begin{pmatrix} 1 \\ \mp i \end{pmatrix} \quad (1.23)$$

Both polarizations can be obtained, with intensity ratios depending on the birefringence δ . We observe that the second term carries a $e^{\mp 2i\theta}$ phase term, which depends on polarization and θ , it is therefore called geometric phase (Φ_G); while the $e^{i\frac{\delta_x+\delta_y}{2}}$ term is the dynamic phase (Φ_D) and it is given by the meta-atom shape and size. In order to fully exploit both, we should avoid the first contribution by restraining $\delta = \pi$, that is, the birefringent

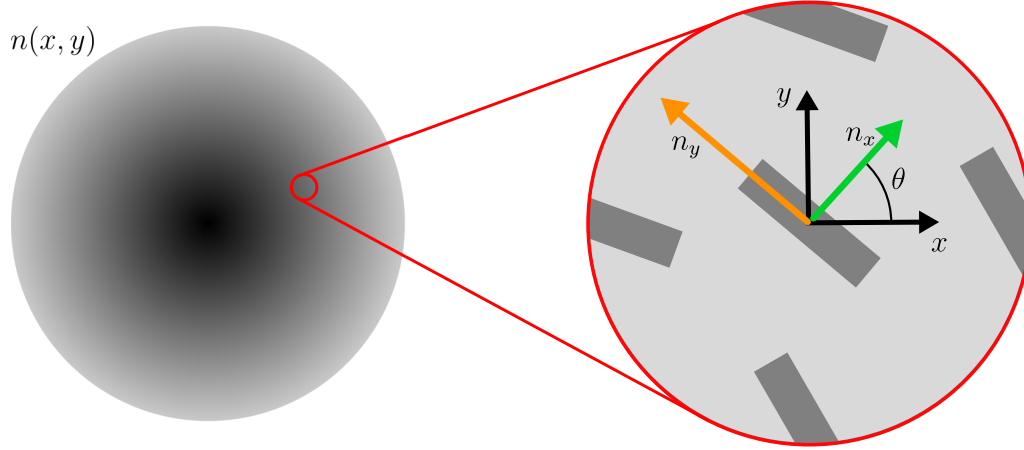


Figure 1.3: A space-varying $n(x, y)$ originating from an array of rotated anisotropic nanostructures. If all meta-atoms are equal, only geometric phase contributes to the phase profile.

medium should act as an half-wave plate. We obtain then:

$$T_{\theta} J_i \Big|_{\delta=\pi} = -i e^{i\Phi_D} e^{\mp i\Phi_G} \begin{pmatrix} 1 \\ \mp i \end{pmatrix} \quad (1.24)$$

$$\text{dynamic phase : } \Phi_D = \frac{\delta_x + \delta_y}{2} \quad (1.25)$$

$$\text{geometric phase : } \Phi_G = 2\theta \quad (1.26)$$

Now, by modulating shapes, sizes and rotations of birefringent nanostructures over a surface, we get two contribution to the phase profile: $\phi(x, y) = \Phi_D(x, y) \mp \Phi_G(x, y)$, where the sign of Φ_G depends on the handedness of the input polarization. Two arbitrarily complex transformations $\phi_L(x, y), \phi_R(x, y)$ can therefore be applied to beams with opposite polarization, by imposing:

$$\Phi_D(x, y) = \frac{\phi_L(x, y) + \phi_R(x, y)}{2} \quad (1.27)$$

$$\Phi_G(x, y) = \frac{\phi_L(x, y) - \phi_R(x, y)}{2} \quad (1.28)$$

Some requirements are to be met:

- Nanostructures must act as half-wave plates, $\delta_y - \delta_x = \pi$, otherwise the first term in Equation 1.23 is not suppressed;
- T_0 in Equation 1.20 assumes a perfect transmittance both for x and y polarizations, in practice such condition cannot be reached, but it is still required at least that the two transmittances should be equal, $T_x = T_y$, a difference would again lead to a not-suppressed first-term;

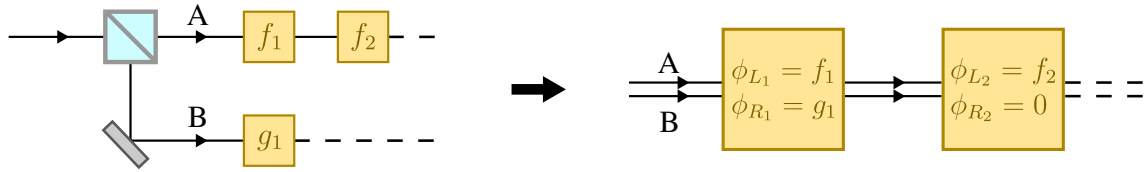


Figure 1.4: Scheme of a two-beamline system reduced into a one-beamline one.

- Φ_D and Φ_G must cover the $[-\pi, \pi]$ interval in order to reach all possible optical functions. The task is straightforward for Φ_G as θ ranges over $[-\pi/2, \pi/2]$, while for Φ_D one should find a suitable set of meta-atoms, each with a different Φ_D , globally covering the $[-\pi, \pi]$ range.

Generally speaking, the first term is hardly annihilated, its presence is referred as "zeroth-order" of the metalens.

1.3 Definition of the to-be fabricated metalenses

Being able to manage independently orthogonal polarization states of light, bifunctional metalenses may multiplex two beamlines into one. For example, let's consider an optical set-up as shown in Fig. 1.4. A beam is split into two branches, A and B, which then undergo different optical operations, f_i and g_i . If such operations can be encoded into metalenses, then it is possible to make A and B coaxial by encoding f_i and g_i as $\phi_{L,S}$ and $\phi_{R,S}$ of bifunctional metalenses, resulting in a more compact system. Since A and B have orthogonal polarization, ideally there is not crosstalk between them. This may prove useful, for example, in STED microscopy or in the generation of vector-beams.

As a proof of concept, two bifunctional metalenses have been designed and fabricated in this work. They combined high-NA (0.38) focusing and LG modes generation in the following way:

$$\text{ML1: LCP: } f_{1L} = 500\mu\text{m}, l_{1L} = -1; \text{RCP: } f_{1R} = 500\mu\text{m}, l_{1R} = +1;$$

$$\text{ML2: LCP: } f_{2L} = 500\mu\text{m}, l_{2L} = +3; \text{RCP: } f_{2R} = 1000\mu\text{m}, l_{2R} = +1;$$

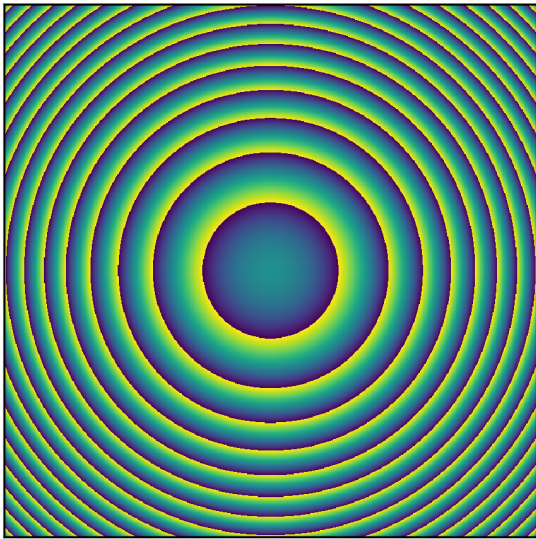
where f s are focal lengths and l s are LG-state numbers, while p were set to 0. The encoded phase profiles were then:

$$\phi_{iL,R}(x,y) = l_{iL,R} \arctan\left(\frac{y}{x}\right) - \frac{2\pi}{\lambda} (\sqrt{x^2 + y^2 + f_{iL,R}^2} - f_{iL,R}) \quad (1.29)$$

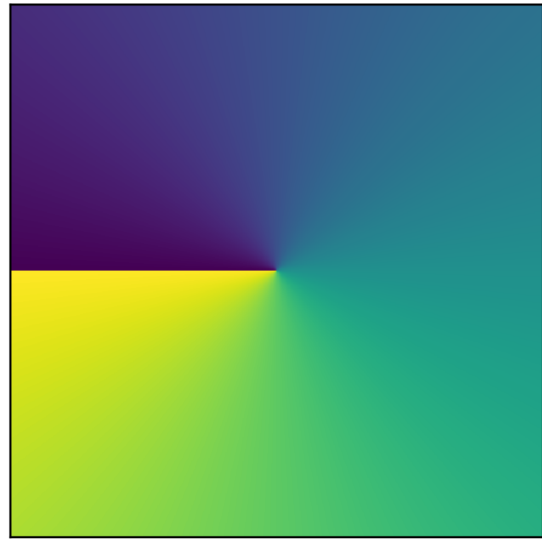
where λ is the wavelength, set at 1310 nm. Dynamic and geometric phases of such metalenses are shown in Fig. 1.5.

Figure 1.5: Colormaps of dynamic and geometric phases of the selected metalenses. Size of the image corresponds to $200\mu\text{m}$ and colors ranges $[-\pi, \pi]$ from dark to light.

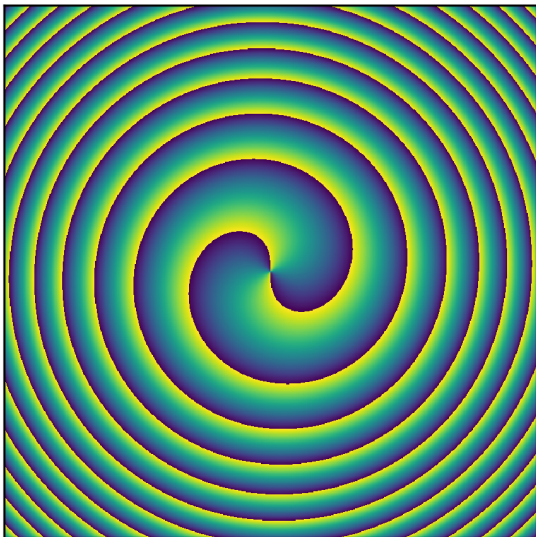
(a) Dynamic phase of ML1



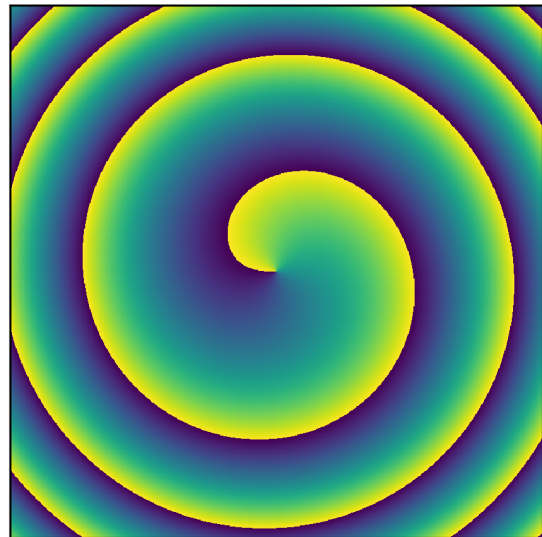
(b) Geometric phase of ML1



(c) Dynamic phase of ML2



(d) Geometric phase of ML2



Chapter 2

Design of metalenses

In this chapter the design of metalenses carried through computational methods is covered. There are two steps required in order to get the final Computer Aided Design (CAD), plus a further simulation of the designed device:

- **Design of meta-atoms**, in which the transmission properties of nanostructures are calculated, so that a group of them, matching the constraints defined at the end of § 1.2, can be selected. Further requirements are demanded by the fabrication process:
 - All meta-atoms have to share the same height of the pillar and period;
 - The width of ridges and ditches should be greater than $\sim 100\text{nm}$.
 - Design pattern no bigger than $500\ \mu\text{m}$.
- **Mapping of meta-atoms**, the selected group of nanostructures is then mapped on the (virtual) surface by matching the needed phase-delay profile. The process should output a file containing the desired pattern in a format intelligible by fabrication softwares.
- **Simulation of the device**, the phase profile of the designed device differs from the theoretical one, so a simulation of light propagation after encountering the designed device is needed for rigorousness.

2.1 Design of meta-atoms

2.1.1 Setting of FEM simulations

Because of the many requirements that need to be met, simple pillars with rectangular section are not enough in order for the dynamical phase to cover the entire $[-\pi, \pi]$ interval. Finite Element Method (FEM) had proven being a flexible and robust algorithm for

calculating the numerical solutions of differential equations; by solving wave equations, the transmission properties of arbitrarily-shaped nanostructures can be obtained. FEM has been employed in this work using commercial software (COMSOL Multiphysics). The simulation box for TE transmission has been built in the following way (Fig. 2.2a):

- Substrate layer made of silicon ($n_{Si} = 3.5030$) and thick $t_{sub} = 1.5\lambda_0/n_{Si}$;
- Nanostructure made of silicon;
- Air ($n_{air} = 1$) layer thick $t_{air} = \lambda_0$;
- Rational Perfectly Matched Layers below the substrate and above the air, both thick $\lambda_0/3$ and having a refractive index equal to the adjacent domain. These domains absorb the electromagnetic field and are necessary in order to avoid spurious internal reflections;
- Input periodic port located $\lambda_0/3$ below the upper PML, with input field parallel to the x dimension of the system ($\hat{\mathbf{E}}_{in} = \hat{\mathbf{x}}$) and $P_{in} = 1W/mm^2$;
- Output periodic port on the lower PML / Substrate boundary, output field aligned with the x direction ($\hat{\mathbf{E}}_{out} = \hat{\mathbf{x}}$);
- Floquet Periodic boundary conditions on the sides of the box.

The corresponding TM configurations have been set by rotating the system by 90° . Meshes were then automatically generated by COMSOL Multiphysics, their optimal fineness have been checked by comparing results (phase delay and transmittance) obtained using different settings of "Physics-controlled"-generated meshes (Fig. 2.1). "Fine" element size has been chosen at last (Fig. 2.2b), as it provides good enough results. Finally the wave equation:

$$\nabla \times (\nabla \times \mathbf{E}) - k_0^2 \epsilon \mathbf{E} = \mathbf{0} \quad (2.1)$$

has been solved by the software; an example of the calculated field is shown in Fig. 2.2c. COMSOL Multiphysics provides a way for calculating transmission properties by means of S parameters. For a generic linear system, each surface through which electromagnetic energy can enter or exit is defined as a port. We can assign to each port i an incident field $E_{in,i}$ and an outgoing field $E_{out,i}$. The S-matrix is the linear map that relates incident and outgoing fields:

$$\begin{pmatrix} E_{out,1} \\ \vdots \\ E_{out,N} \end{pmatrix} = \begin{pmatrix} S_{11} & \dots & S_{1N} \\ \vdots & \ddots & \vdots \\ S_{N1} & \dots & S_{NN} \end{pmatrix} \begin{pmatrix} E_{in,1} \\ \vdots \\ E_{in,N} \end{pmatrix} \quad (2.2)$$

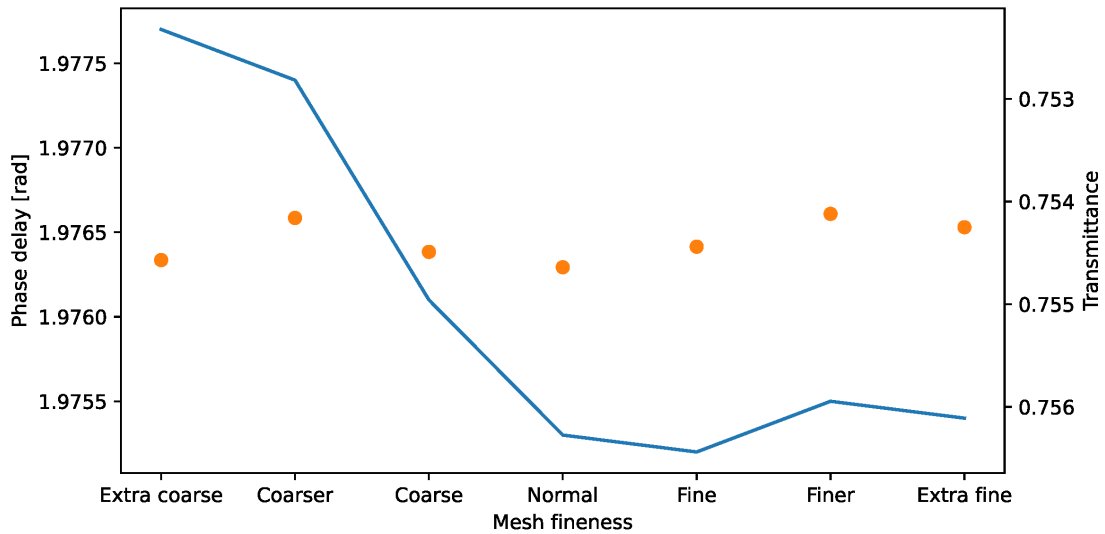


Figure 2.1: Plots of transmittance and phase delay resulting from the same geometry and different mesh sizes. Phase delays show a converging behaviour, while transmittances don't. Variations of both are negligible compared to their absolute values.

According to the COMSOL Documentation^[28], if there's only one $E_{in,i} \neq 0$, let's say Port 1, the S parameters are obtained from the calculated field \mathbf{E}_c by:

$$S_{i1} = \frac{\int_{\text{port } i} (\mathbf{E}_c \cdot \mathbf{E}_{out,i}^*) dA_i}{\int_{\text{port } i} (\mathbf{E}_{out,i} \cdot \mathbf{E}_{out,i}^*) dA_i} \quad (2.3)$$

In our system we have indeed one Input Port (1) and we are interested in the coefficient that relates its incident field and the outgoing field of the Output Port (2), that is S_{21} . Transmittance and phase delay can then be calculated as:

$$T = |S_{21}|^2 \quad (2.4)$$

$$\delta_x = \arg(S_{21}) - k_0 n_{Si} t_{sub} - k_0 n_{air} t_{air} \quad \arg(S) = \arctan\left(\frac{\Im[S]}{\Re[S]}\right) \quad (2.5)$$

After simulating both TE and TM configurations, from which we respectively obtain δ_x and δ_y , dynamic phase of the meta-atom can be finally computed as in Equation 1.25.

2.1.2 Results of simulations

Once the computational protocol for obtaining the transmittance and phase delay from a geometry had been defined and validated, many trials with different periods, heights and shapes, were executed in order to get a group of suitable meta-atoms. The choice of pillar's section was arbitrary as long as the requirements were met. The metrics used for

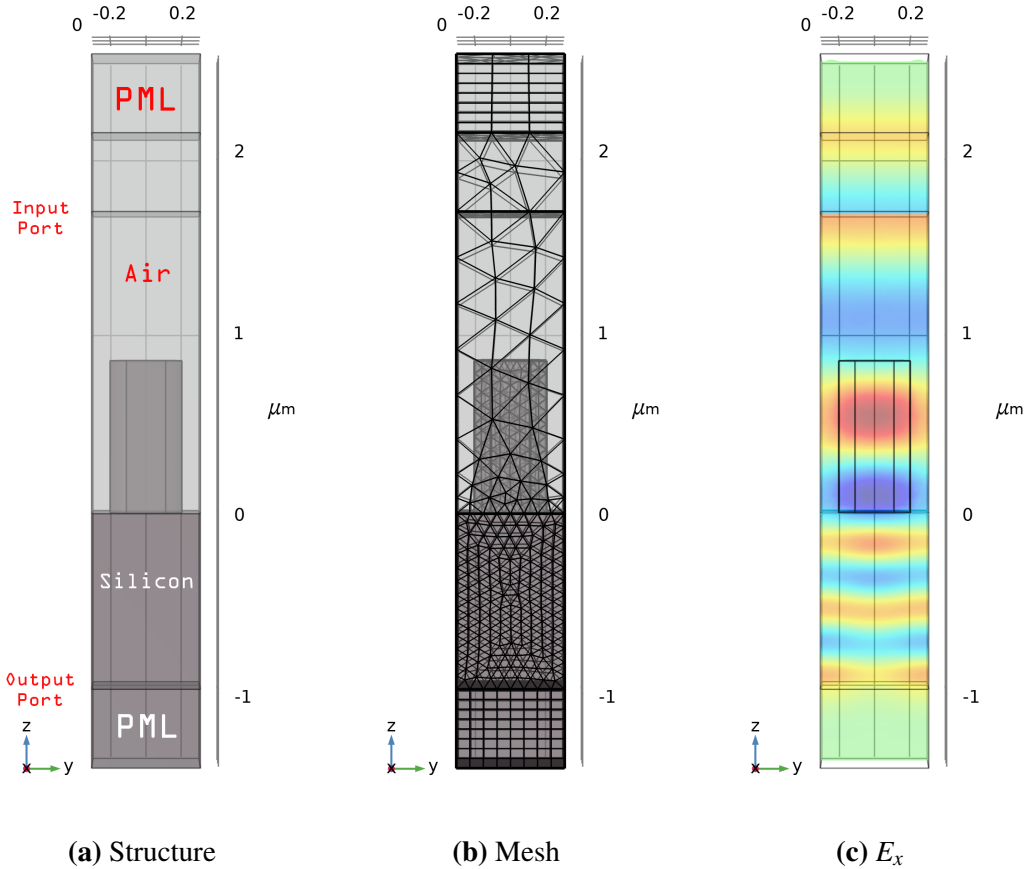


Figure 2.2: Structure, mesh and calculated E_x of a meta-atom geometry. Mesh in silicon is denser than in air because of the higher refractive index, which leads, as it can be seen from the field plot, to a decrease in the wavelength. Inside Perfectly Matched Layers we observe the exponential decay of the transmitted and reflected field, as required.

accepting a meta-atom were:

$$\Delta T = |T_y - T_x| < 0.03 \quad (2.6a)$$

$$\Delta \phi = |\delta_y - \delta_x - \pi| < 0.3 \quad (2.6b)$$

$$\bar{T} = \text{mean}(T_y, T_x) > 0.7 \quad (2.6c)$$

Given a suitable meta-atom with $\Delta \phi \sim 0$ and Φ_D , another one with $\Phi'_D = -\Phi_D$ could be easily found by a 90° rotation, therefore the coverage of Φ_D actually had to fill a $[0, \pi]$ interval only.

The search was not carried by a simple brute force approach. For example, a rectangular section has four degrees of freedom (length, width, height, period); a brute force approach of simulating each combination of a 4-dimensional mesh, even for a coarse mesh of 10 values per dimension, would had needed 10^4 trials. Considering that each trial took 30 seconds, this coarse exploration of the degree-of-freedom space (DOF space) of one shape would had taken three and a half days. Since period and height were to be shared by all

to-be-selected meta-atoms, first attempts were made to reduce their range and eventually fix their values, in order to lower the dimensionality of DOF space. A very coarse mesh of 4 values per dimension ($4^4 = 256 \rightarrow \sim 2$ hours) had been used, the best values of the first mesh were then adopted for a second finer mesh, results are shown in Fig. 2.3. At that point it became clear that finer grids were required for width and length in order to further refine the parameters.

Results for a refined mesh are reported in Fig. 2.6a. From data of rectangular shapes, a "belt" of high \bar{T} and low $|\Delta T|$ appears for length \cdot width $\simeq 50000\text{nm}^2$. By tuning period and height with a trial-and-error approach, one side of the $\Delta\phi \simeq 0.0$ domain was made to coincide with the belt, and some first good candidates were obtained at period = 600 nm and height = 850 nm.

In order to further validate the computing protocol, a test on geometric phase of a suitable shape was performed. In this test the relation between rotation angle of the pillar θ and total phase delay Φ was verified for an impinging LCP field on the Input port and a RCP field on the Output port. Such relation should be:

$$\Phi = \Phi_G + \Phi_D = 2\theta + \Phi_D. \quad (2.7)$$

Except for the I/O fields, every other setting was kept the same as before. Φ has been evaluated for a rectangular pillar $110\text{nm} \times 440\text{nm}$ at 10 different θ s from 0° to 90° . From the simulation results, a linear fit $\Phi = a + b\theta$ was executed, as shown in Fig. 2.4. Linear coefficient was doubtless compatible with Equation 2.7 and the fit was rather good. From the residuals, a clear cosine-like contribute emerged, which may be due to angle-dependent resonances. Considering that geometric phases ranged from -180° to 180° , while these deviations reach 3° at most, they were considered negligible.

In order for Φ_D to cover the $[0, \pi]$ interval, many different sections were then tried; finally rectangular, elliptical and "coffee bean" (CB) sections, depicted in Fig. 2.5 with their degrees of freedom, fulfilled the task. CB meta-atoms displayed in general higher transmittances and lower $|\Delta T|$ s, as shown in Fig. 2.6b, enabling them to cover a large interval of Φ_D .

Figure 2.3: $\Delta\phi$ for the first and second meshes of height, period, width and length values for the rectangular shape. Axes of subplots represents widths and lengths of rectangles, expressed in nanometers. The red square enhances the chosen interval from data of the first in order to generate the second. Periods and heights in the range $\sim 600 - 650$ nm and $\sim 800 - 950$ nm seems equivalent at this mesh resolution.

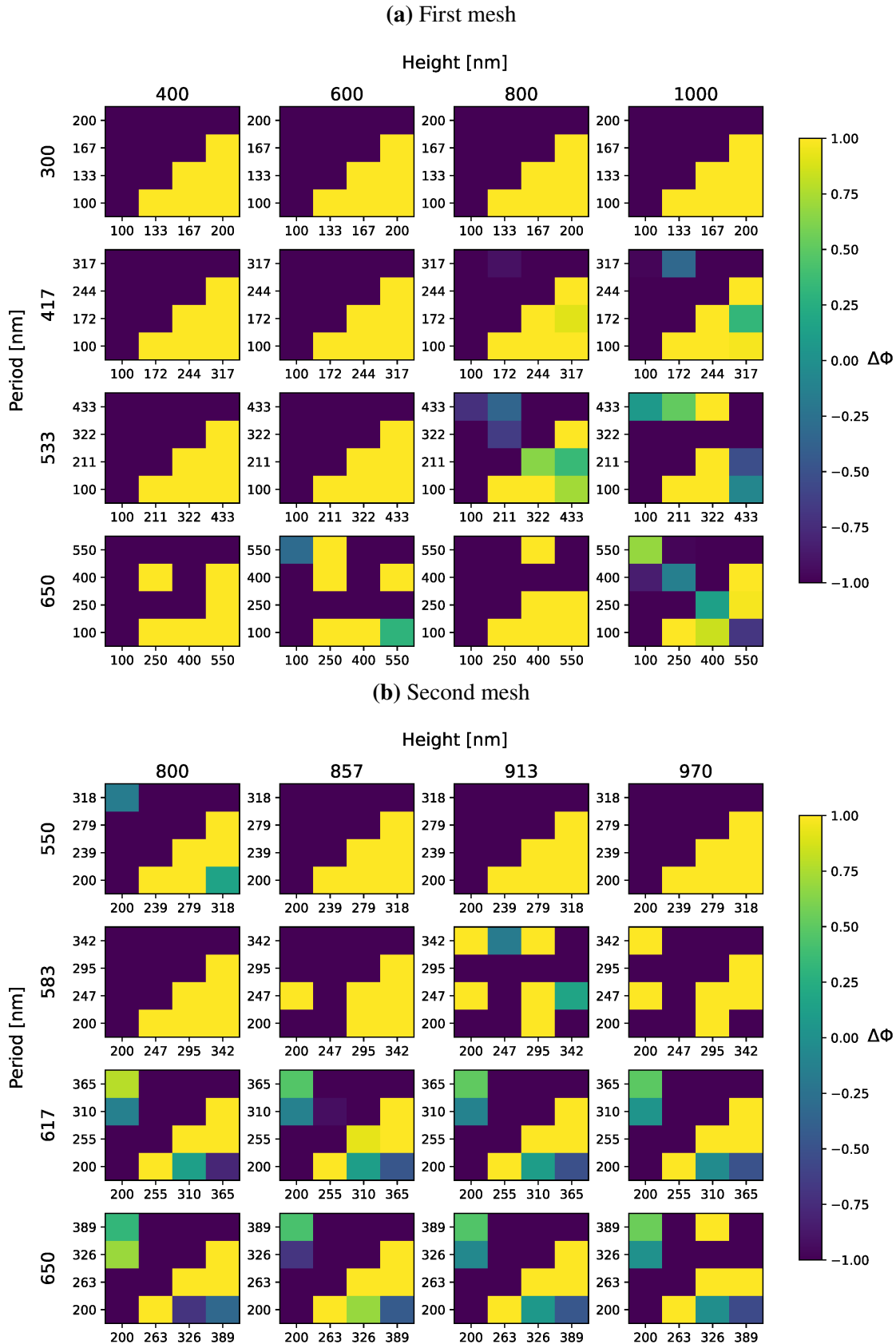


Figure 2.4: On the left, the phase delays Φ evaluated at different rotation angles θ . Linear fit is rather good and the angular coefficient is compatible with the theoretical value 2. On the right, residuals from the linear fit are plotted against θ ; the cosine-like trend suggests a more complex model would be required for a fine description of $\Phi(\theta)$, but it is not very relevant for our purposes.

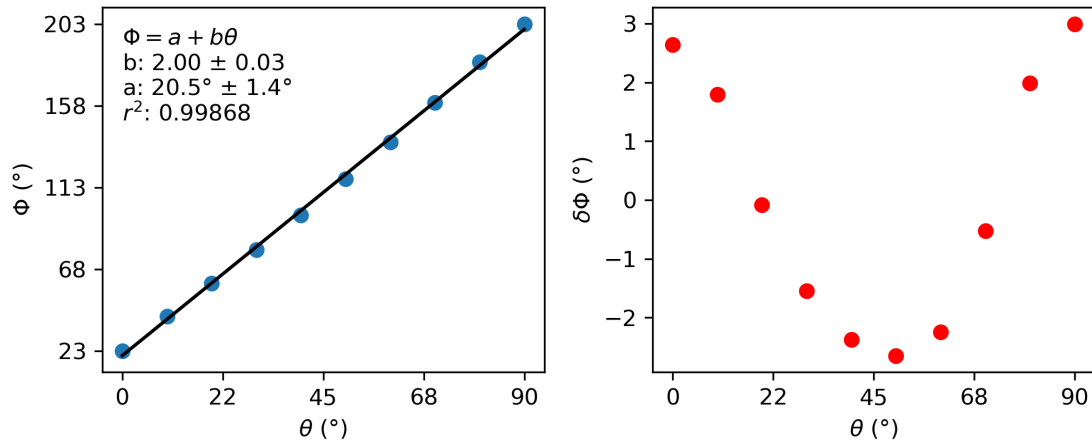


Figure 2.5: Nanostructure-section types among the selected meta-atoms. Regarding CB, radius r and distance $dist$ have been set $r = (\text{period} - 100\text{nm})/2$ and $dist = \text{period}/4$.

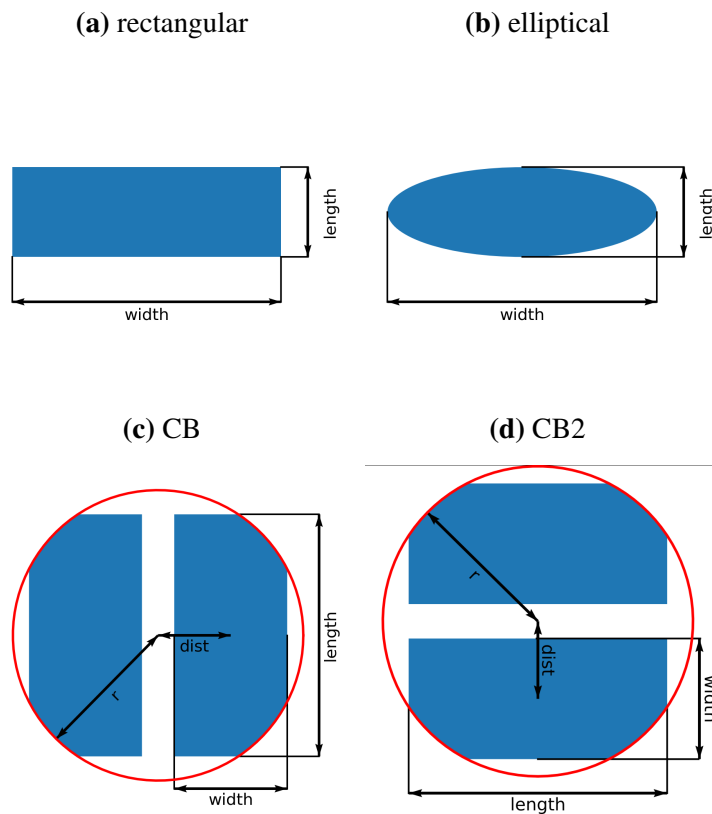
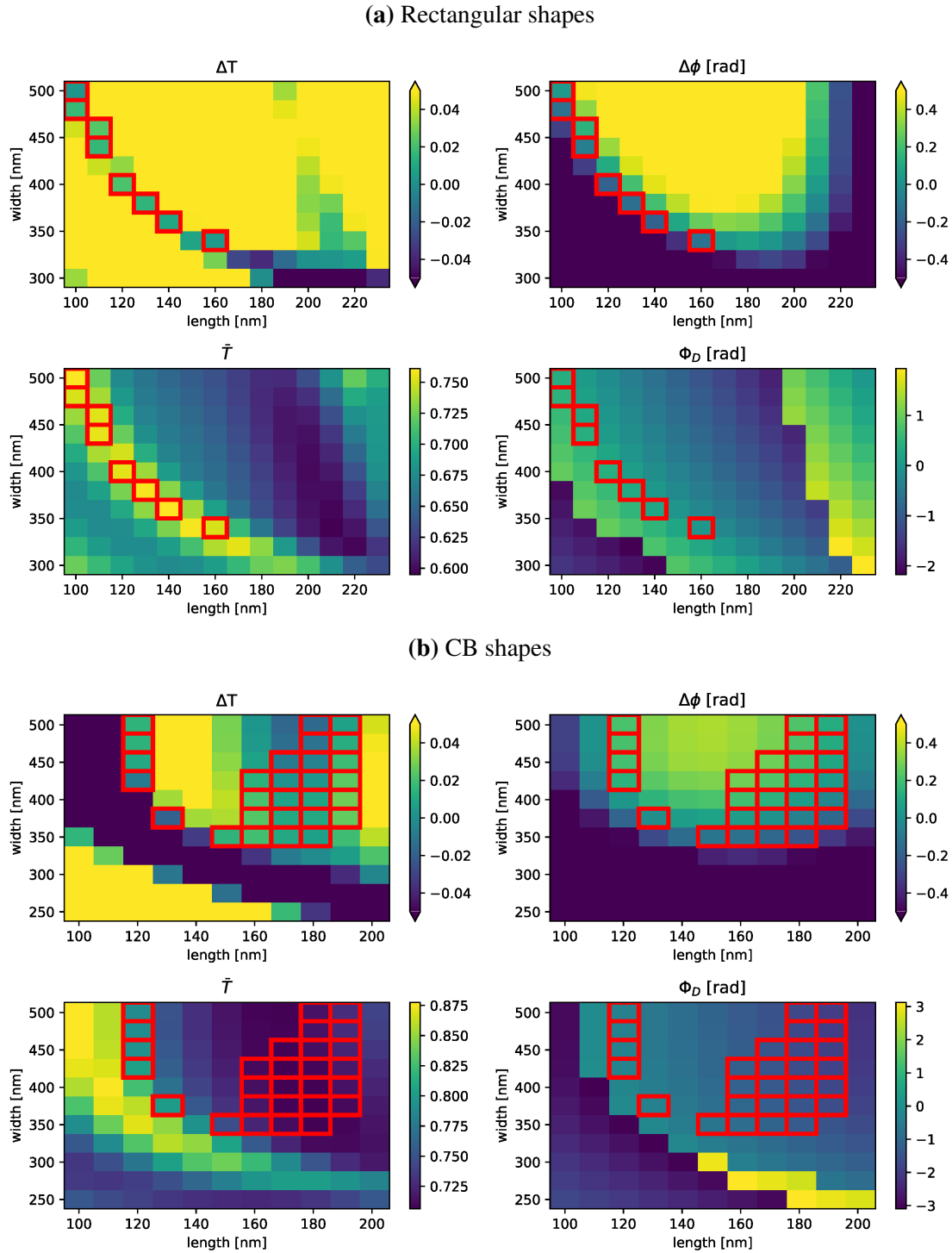


Figure 2.6: Results of simulations for rectangular and coffee bean shapes with height = 850 nm and period = 600 nm. Each coordinate in the colour-maps represent one cross-section, colours identify the property represented in the maps. Red rectangles identifies good candidates based on requirements defined in 2.6



Wavelength = 1310 nm, Period = 600 nm, Pillar height = 850 nm						
n	type	width(nm)	length(nm)	$\Delta\phi$	$\Phi_{D,n}$	\bar{T}
1	ell	400.00	170.00	-0.03	-3.06	0.76
2	rect	480.00	100.00	-0.13	-2.66	0.75
3	CB	190.90	501.00	0.12	-1.97	0.73
4	CB	180.80	400.60	0.06	-1.55	0.71
5	CB	160.60	400.60	0.20	-1.13	0.71
6	CB	150.50	350.40	0.11	-0.68	0.75
7	ell	190.00	380.00	0.08	-0.14	0.74
8	rect	100.00	480.00	0.13	0.49	0.75
9	CB2	190.90	501.00	0.12	-1.97	0.73
10	CB2	180.80	400.60	0.06	-1.55	0.71
11	CB2	160.60	400.60	0.20	-1.13	0.71
12	CB2	150.50	350.40	0.11	-0.68	0.75
13	ell	380.00	190.00	-0.08	3.00	0.74

Table 2.1: Set of nanostructures that meet the constrains and whose dynamic phase cover the $[-\pi, \pi]$ interval. The types of meta-atoms and their parameters are shown in Fig. 2.5

2.2 Mapping of meta-atoms

More than 100 suitable meta-atoms were found, from which a set M of 13 meta-atoms $MA_n, n \in \{1, \dots, 13\}$ were selected for practical purposes. Their properties are collected in Table 2.1.

The quality of the phase profile is not severely affected by such discretization, as shown in § 2.3. Mapping $\Phi_D(x, y) \rightarrow MA_n$ and parsing into .gds²[1] or .asc files, the file formats accepted by the EBL machine, was carried out by a script written in Rust programming language. Those file formats encode the structures' geometries through lists of their boundaries, expressed as ordered sets $S_i = \{(x_j, y_j), x, y \in \mathbb{Q}\}$ of coordinates.

First, the boundaries B_n of our MA_n were defined as sets of coordinates $\{(u_j, v_j) \mid u_j, v_j \in [-\tau/2, \tau/2]\}$, with u, v space being isometric to x, y . Then, (x, y) space was discretized into a square lattice of (x_i, y_i) points, spaced $\tau = 600\text{nm}$ apart. On each (x_i, y_i) , the best MA was chosen and placed:

1. **Choice of MA_n :** For each location, the best meta-atom would be the one whose dynamic phase Φ_D, n is the closest to the theoretical one $\Phi_D(x, y)$. Generally speaking, $\Phi_D(x, y)$ spans over \mathbb{R} , but from a physical point of view $\Phi + 2\pi$ is equivalent to Φ . Therefore, the metric $d(\Phi, \Phi')$, which must be defined in order to select the best local MA

$$MA_n : \min_{n \in \{1, \dots, 13\}} \{d(\Phi_D(x_i, y_i), \Phi_{D,n})\}, \quad (2.8)$$

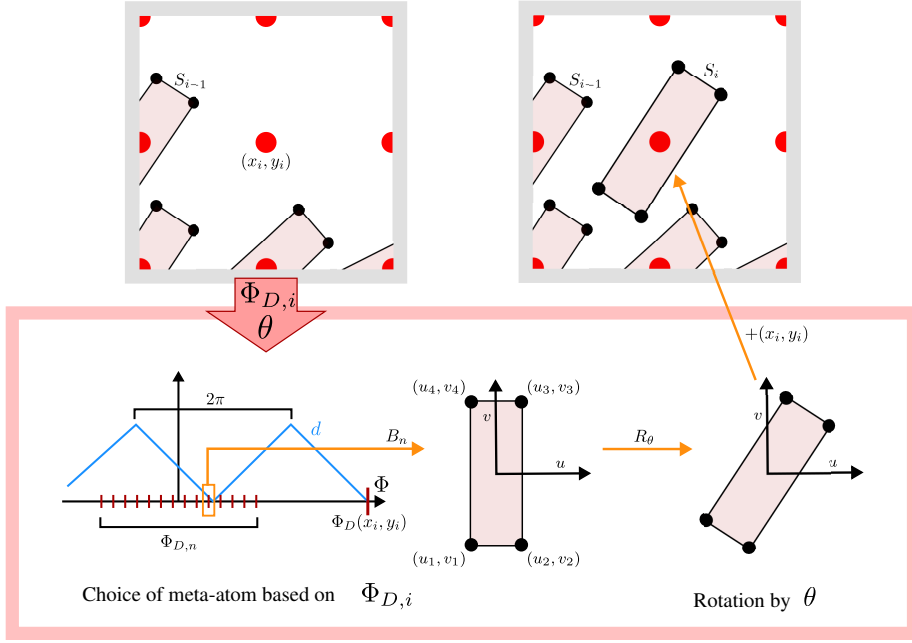


Figure 2.7: Scheme of meta-atom mapping on (x_i, y_i) . First, Φ_D and θ are calculated for the given coordinate, then the best meta-atom is selected, finally its boundary points are rotated and shifted in regard to the coordinate

had to be accordingly periodic. A triangle function was employed as a metric:

$$d(\Phi, \Phi') = |(\Phi' - \Phi + \pi) \% 2\pi - \pi| \quad (2.9)$$

where $\%$ is the modulo operation based on Euclidean division. The chosen metric acts as $|\Phi' - \Phi|$ in the interval $[-\pi + \Phi, \pi + \Phi[$ and repeats outside with period 2π , therefore its minima are located at $|\Phi' - \Phi| = 2m\pi, m \in \mathbb{Z}$.

2. **Placing:** The placing operation consisted in the addition of S_i to the global list of boundaries, S_i computed as:

$$S_i = \{(x_j, y_j) : (x_j, y_j) = R_{\theta_i}[(u_j, v_j)] + (x_i, y_i), (u_j, v_j) \in B_n\} \quad \theta_i = \frac{\Phi_G(x_i, y_i)}{2} \quad (2.10)$$

where $R_{\theta}[\cdot]$ is the rotation of \cdot by θ , and B_n is the boundary set of the selected MA_n . Meta-atoms can have more than one boundary, as in the CB shape; if their (u, v) sets share the same base origin, it is enough to repeat the placing operation for each boundary of the the meta-atom.

A graphical representation of these operations is depicted in Fig. 2.7. Finally, S_i sets were parsed according to .gds2 or .asc format. The former is a binary file format and required an external library^[15]. A draft from a generated pattern is depicted in Fig. 2.8.

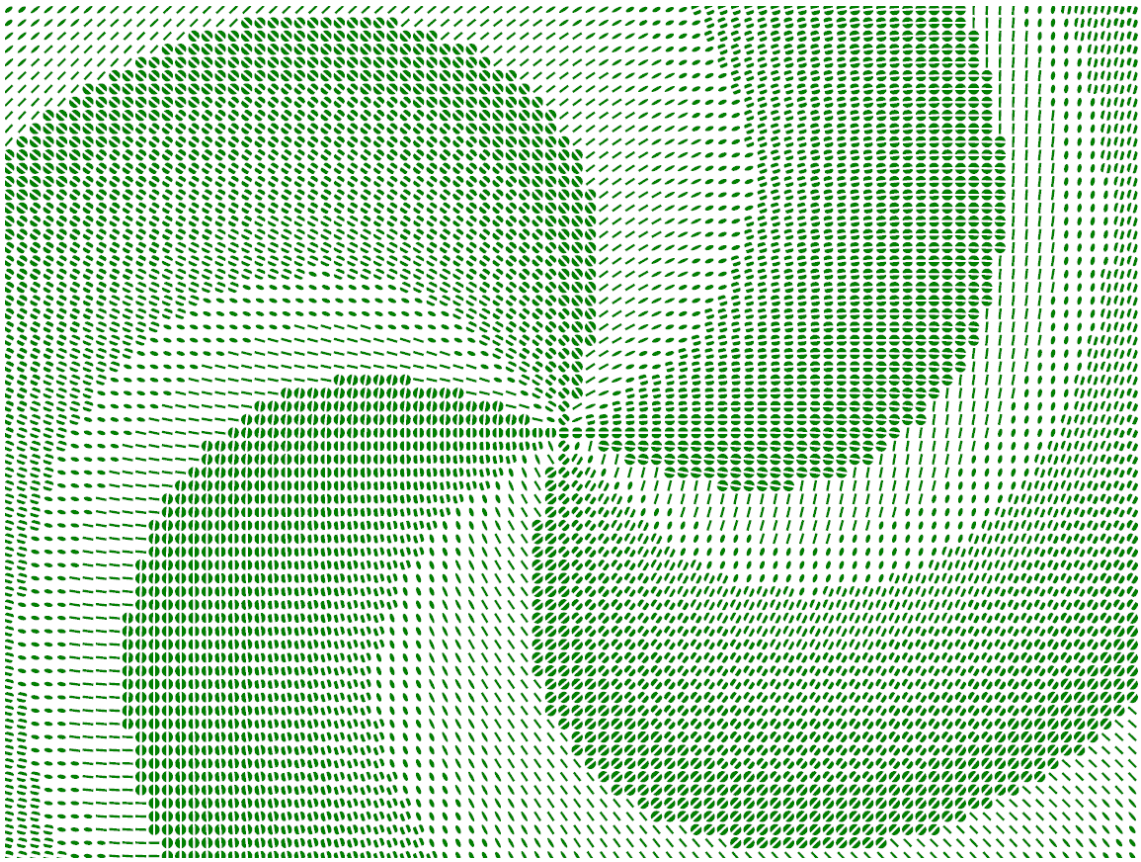


Figure 2.8: Detail of the resulting pattern of ML2 in the gds2 file.

2.3 Simulation of the devices

The phase profile of the designed device differs from the theoretical one. The main difference is due to discretization both of the metalens plane, going from $\{(x, y) \in \mathbb{R}^2\}$ to $\{(x_i, y_j) \in \mathbb{Q}^2, x_i - x_{i-1} = \tau\}$, and of the phase space, from $\{\phi \in [-\pi, \pi[]\}$ to $\{\phi_1, \phi_2, \dots, \phi_{13}; \phi_i \in [-\pi, \pi]\}$. The concept is similar to rasterisation in computer graphics. The issue could be relevant where the theoretical phase profile is very steep, leading to a local under-sampling of the profile. Therefore, simulations of light propagation have been performed in order to assess the design.

The theoretical framework underlying these simulations is Fourier optics, which describes propagation of light by means of Fourier transforms and linear systems.

2.3.1 Fourier optics

A system which maps an input $f_1(t)$ to an output $f_2(t)$, is defined linear if it satisfies the relation:

$$f_2(t) = \int h(t; \tau) f_1(\tau) d\tau \quad (2.11)$$

where $h(t; \tau)$ is called the impulse response function of the given system. It is also said shift-invariant if, when its input is shifted in t , the output shifts by an equal t . Then, its impulse response function only depends on the difference $t - \tau$: $h(t; \tau) = h(t - \tau)$, therefore:

$$f_2(t) = \int h(t - \tau) f_1(\tau) d\tau \quad (2.12)$$

By applying the convolution theorem of Fourier transforms, the last equation can be written as:

$$F_2(\mathbf{v}) = H(\mathbf{v}) F_1(\mathbf{v}) \quad (2.13)$$

where F_2, F_1, H are the Fourier transforms of f_1, f_2, h , respectively; $H(\mathbf{v})$ is called the transfer function of the system.

Regarding optics, one polarization component of the electromagnetic field entering an optical system can be described as a complex function $U(x, y; z = 0)$. Propagation in free space must satisfy the Helmholtz Equation 1.9, thus free-space is a linear system; since it is independent of the coordinate system, it is also shift-invariant. Therefore the output $U(x, y; z = d)$ can be calculated:

$$U(x, y; z = d) = \text{FT}^{-1}[F(\mathbf{v}_x, \mathbf{v}_y, z = d)] \quad (2.14)$$

$$F(\mathbf{v}_x, \mathbf{v}_y, z = d) = H(\mathbf{v}_x, \mathbf{v}_y; d) F(\mathbf{v}_x, \mathbf{v}_y, z = 0) \quad (2.15)$$

where $F(\mathbf{v}_x, \mathbf{v}_y, z = 0) = \text{FT}[U(x, y; z = 0)]$.

Let us find the transfer function of free-space. Assuming the beam is monochromatic,

each of its Fourier components $F(v_x, v_y) \exp[-j2\pi(v_x x + v_y y)]$ can be seen as the contribution of a plane wave $F(v_x, v_y) \exp[-j(k_x x + k_y y + k_z z)]$, where $k_x = 2\pi v_x$, $k_y = 2\pi v_y$, and $k_z = \pm 2\pi \sqrt{\lambda^{-2} - v_x^2 - v_y^2}$. The sign of k_z is such that $k_x^2 + k_y^2 + k_z k_z^* = (2\pi\lambda^{-1})^2$, it should be negative for $v_x^2 + v_y^2 > \lambda^{-2}$. Propagation of $U(x, y)$ can then be described by the propagation of its plane wave components along z , therefore:

$$H(v_x, v_y; d) = \exp(-jk_z d) = \exp(\mp j2\pi d \sqrt{\lambda^{-2} - v_x^2 - v_y^2}) \quad (2.16)$$

2.3.2 Simulation algorithm and results

The propagation algorithm for RCP polarization was laid out as follows:

- **Construction of the input field** $U(x, y; z = 0)$. The number of meta-atoms along one direction (metalens size / period) was taken as the size of the input 2D array. To each (n, m) entry of the array was assigned the complex number $\hat{T}_i \exp(j\phi_i^{RCP})$, where \hat{T}_i, ϕ_i^{RCP} are the transmittance and the RCP phase delay of the meta-atom i assigned to position n, m . The array was then multiplied by the field profile of a gaussian beam of width $100\mu\text{m}$.

The output array had the same space resolution of the input; since the resulting intensity spots required higher resolutions, the input resolution could be augmented by a factor r through the Kronecker product of the input matrix with a 1-filled square matrix of size r . Each entry would be mapped to a r -sized block of the transformed matrix. For example, the "augmentation" of a matrix \mathbf{A} with factor $r = 2$:

$$\mathbf{A} \otimes \begin{pmatrix} 1 & 1 \\ 1 & 1 \end{pmatrix} = \begin{pmatrix} a_{11} & a_{11} & \dots & a_{1m} & a_{1m} \\ a_{11} & a_{11} & \dots & a_{1m} & a_{1m} \\ \vdots & \vdots & \ddots & \vdots & \vdots \\ a_{n1} & a_{n1} & \dots & a_{nm} & a_{nm} \\ a_{n1} & a_{n1} & \dots & a_{nm} & a_{nm} \end{pmatrix} \quad (2.17)$$

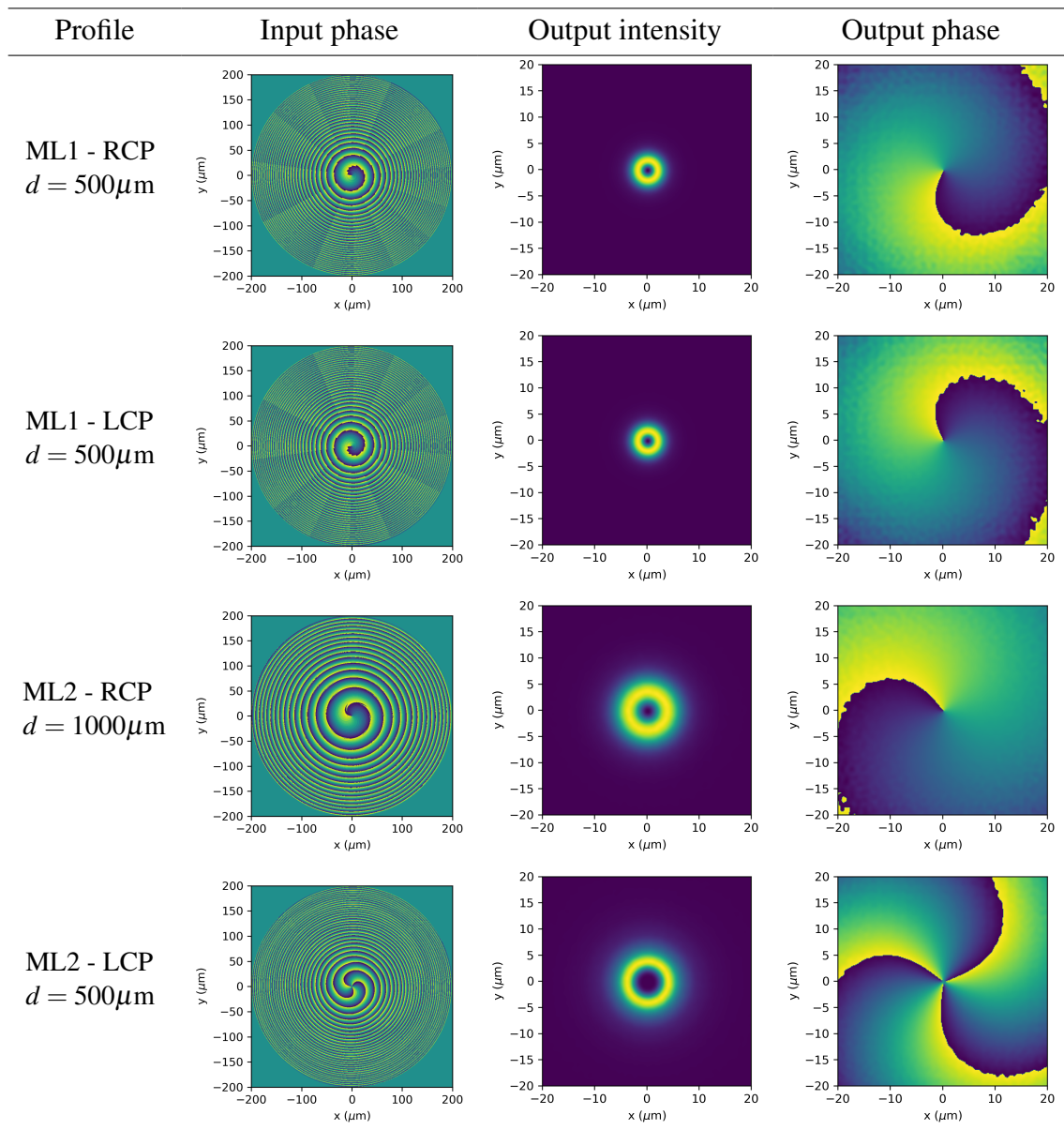
- **Propagation.** A "transfer" 2D array with the same size of the input was constructed, its values as in Equation 2.16. The value of z depended on which metalens was to be simulated. The Fast Fourier Transform was applied to the input array, then it was multiplied by the transfer array and finally brought back with Inverse Fast Fourier Transform.
- **Plotting.** Colormaps of the resulting field intensity and phase were generated and zoomed so that the intensity spots, which were much smaller than the metalenses, had distinguishable features.

The algorithm has been coded in Python. Generated inputs and outputs are shown in Table 2.2.

The doughnuts from ML1 are the same for RCP and LCP polarization, as they should be since they depends on $|l|$ and $|l_{RCP}| = |l_{LCP}| = 1$. The phases are compatible with $l_{RCP} = 1$ and $l_{LCP} = -1$. The $-\pi/\pi$ border clearly shows some deviations from pure states, but since they occur where the intensity is very low, they should be negligible; the same occurs in ML2 phases. Intensity and phase profiles from ML2 are compatible with $l = 1$ and $l = 3$ for RCP and LCP polarizations, respectively. They are both bigger than those from ML1, the former because of its lower numerical aperture, the latter because $l = 3$ doughnuts are inherently wider than $l = 1$ ones.

Simulations therefore confirm the desired functionalities of the designed patterns. A lower state purity may be expected on the borders of the intensity spot.

Table 2.2: Inputs and outputs of simulations. A Gaussian beam has been multiplied by $\exp(j\phi(x,y))$, with $\phi(x,y)$ being the actual metalens phase delay, shown in the "input" column. The output intensities and phases obtained after a propagation d are shown in the respective columns.



Chapter 3

Principles of lithography

Since some fabrication decisions affect multiple fabrication processes, the fabrication issue is split in two: this chapter covers the describing models and general implementation aspects of processes, giving the required knowledge framework upon which implementation choices can be made; those are discussed in the next chapter, which collects all practical details.

3.1 Introduction

In the last decades, the most recognized technological advancements involve miniaturization. Computers, servers and smartphones are made by microchips, integrated circuits whose components are no bigger than 10 nm. Fabrication of such small features would not be feasible without electron beam lithography (EBL), metalenses are no exception. EBL consists in a sequence of fabrication steps, there are many processes that can be involved; only those actually performed in this work, shown in Fig. 3.1, will be explained. Electrons themselves are not able to carve materials efficiently, as ions do in focused ion beam, still, they can deposit a great amount of energy in a limited space. Susceptible materials can change their local chemical properties when exposed to an high-energy electron beam. Silicon, the material of our interest, is not susceptible, therefore a thin film of a polymer, called resist, is first deposited on the surface. After exposure, a wet etching is performed on resist and the desired pattern emerges in the film. Its transfer to the silicon substrate is obtained through reactive ion etching (RIE). Resists are not capable of acting as mask in the process, therefore the deposition of an harder mask is first required, followed by removal of the polymer layer (lift-off).

During layout of the protocol, it is important to keep track of the *tone* of protruding structures, which is positive, if their pattern is equal to the target one, or negative if it is the opposite. There are some operations, such as lift-off, that invert the tone, if their number in the protocol is odd, the writing pattern must be inverted.

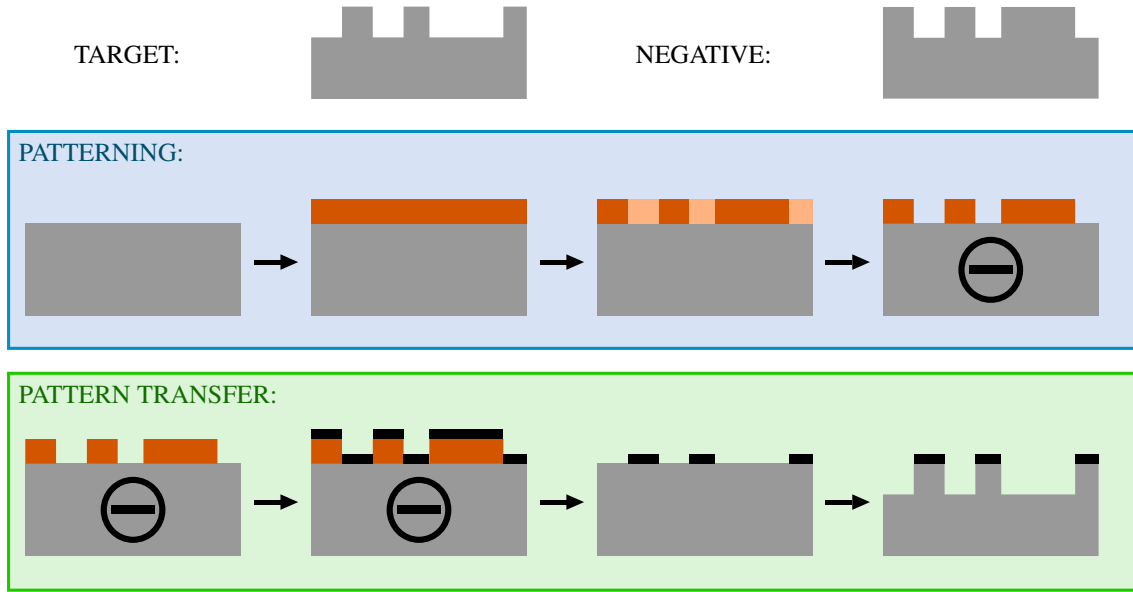


Figure 3.1: Fabrication steps involved in this thesis. The \ominus sign means that the protruding structures exhibit a negative tone.

The whole protocol can be split in two sets of steps: the first, from substrate to developed resist, aims to generate a target pattern, the second, from developed resist to target, transfer the generated pattern from resist to substrate. The subdivision is convenient as each set requires its own parameter-optimization cycles, as will be explained in the next chapter.

3.2 Resists

As anticipated in the introduction of the chapter, resists are materials whose chemical properties change when exposed to high-energy electrons. More precisely, they become more or less vulnerable to etching, which constitutes the development process, in order to be eroded only on specified locations. There are many kinds of resist materials, all of them are polymers, differing in properties and performances. Their working principle is the dependence of the rate of dissolution on molecular chain length. There are many models describing polymer dissolution and it can be generally expressed as^[24]:

$$R_d \propto CM^{-\alpha}\phi_p^{-\beta}, \quad \alpha, \beta > 0 \quad (3.1)$$

where C, α, β are empirical constants, M is the molecular weight and ϕ_p is the polymer volume fraction in the solvent. Generally speaking, the smaller the polymer chains, the greater the dissolution rate. The main classification of resist is based on their behaviour upon electron irradiation, positive or negative. The former gets damaged when hit by high-energy electrons. In the exposed regions carbon chains shorten and therefore ex-

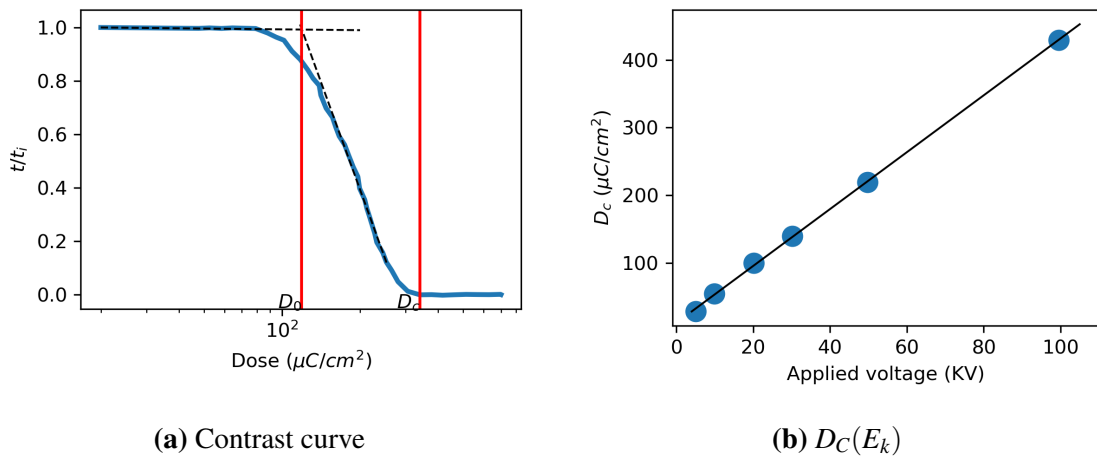


Figure 3.2: Contrast curve and $D_C(E_k)$ for a commercial PMMA resist^[10]

hibit enhanced etching rates during the development process. Carbon chains of the latter, instead, undergo branching and show decreased etching rates. After development, the exposed domain constitutes the ditches in positive resists and the ridges in negative ones. The choice may depend on the processes that follow, which can again invert the tone of image.

The parameters that quantify the quality of a resist are the *contrast* and the *clearing dose*. They are calculated from the contrast curve, the function that relates residual thickness after development and electron dose; for a positive resist it is a monotone decreasing function. The dose at zero residual thickness is the clearing-dose (D_c), that is the amount of electrons (in terms of $\frac{\mu\text{C}}{\text{cm}^2}$) needed to dig the resist down to the substrate. Contrast γ is defined as:

$$\gamma = \frac{1}{\log_{10}(D_c/D_0)} \quad (3.2)$$

where D_0 is the onset of the decreasing function, as shown in Fig. 3.2a. The higher the contrast, the less sensitive is the process to dose variations and greater aspect ratios can be achieved. A lower clearing dose takes less time to be applied, shortening the whole process duration. D_c depends on the energy of incoming electrons E_k , and the relation is roughly linear (Fig. 3.2b). Higher E_k s entail longer processes, but lower E_k s worsen resolution. Since it depends also on other factors (materials, thicknesses, ...), D_c must be determined experimentally. Common values for PMMA are $D_c \sim 320 \frac{\mu\text{C}}{\text{cm}^2}$ and $\gamma \sim 3$.

Another important fact to consider is that of undercut/overcut. After development, walls of ridges are not perfectly vertical but show a finite slope. If the width of ditches is greater near the substrate than on the surface, then it is called an undercut, otherwise it is called an overcut (Fig. 3.3). Depending on working conditions, positive and negative resists can exhibit undercuts or overcuts. Undercuts are very useful when a deposition/lift-off is later applied, as it will be described in § 3.6, while overcuts would be inconvenient.

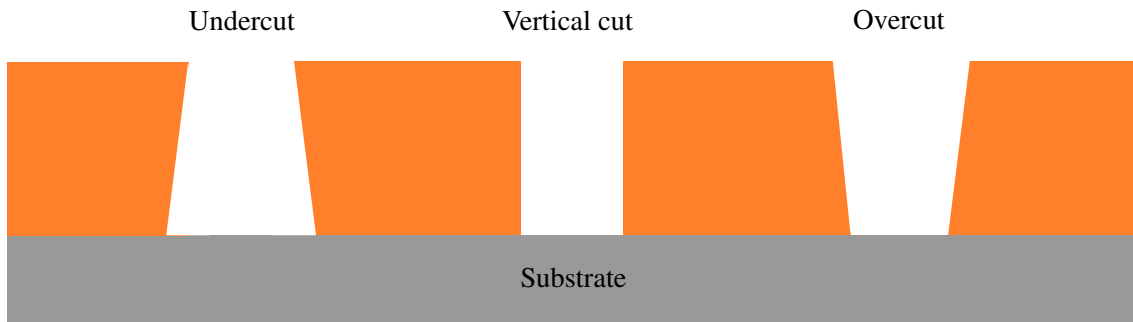


Figure 3.3: Types of cuts after development.

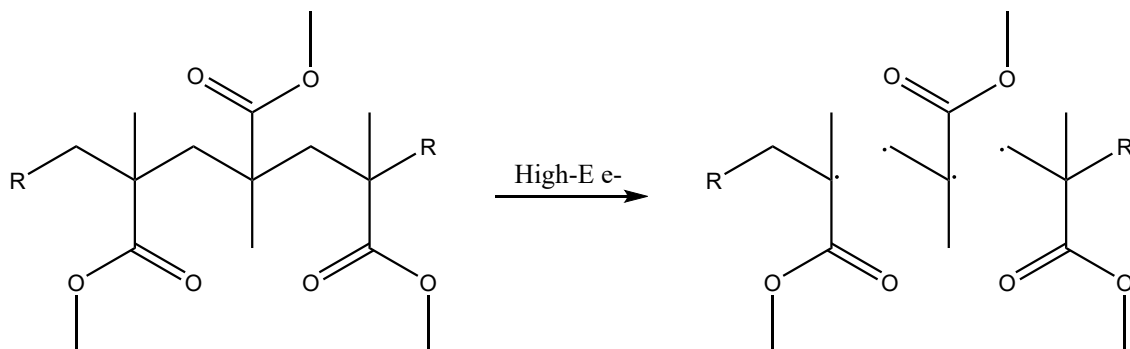


Figure 3.4: Scheme of the PMMA radical fragments generated upon electron irradiation.

In this work, PMMA, a common positive resist with an undercut behaviour, has been used. Upon electron irradiation of PMMA, and similarly for other positive resists, the main chain is cleaved and the molecular mass drops from initially 950 000 g/mol to 5.000–10.000 g/mol. This main chain scission is primarily due to radical processes (Fig. 3.4). At an optimal dose, radicals recombine and form molecules with a molecular mass of about 5 000 g/mol. If however the dose is drastically increased, a large number of radicals are produced and undergo cross-linking so that molecules with higher molecular masses are obtained. PMMA would then turn into a negative resist. For this reason it is advisable not to inspect PMMA with an electron microscope, as prolonged exposure to the electron beam may harden the PMMA and make it difficult to remove. In order to check the development quality, a small reference pattern near the samples is useful can be inspected without affecting the samples.

3.3 Spin coating

Resist deposition is the first and a very delicate step, since defects or stresses can easily arise and compromise product quality. The most common technique adopted for the task is spin coating. A solution of resist in a volatile solvent is sprayed on the substrate, which spins at high speeds (~ 3000 rpm). By doing so, the solution get uniformly distributed and the solvent evaporates, leaving a layer of the resist material behind, as shown in Fig. 3.5.

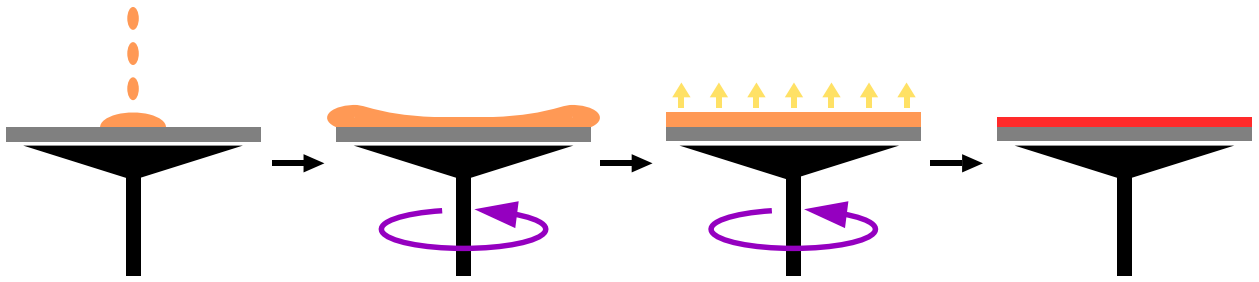


Figure 3.5: Graphical representation of spin coating steps and phenomena.

Thickness and quality of the layer depend on the process conditions, in particular the simple model proposed by Emslie et al. states for thickness^[13]:

$$h = \frac{h_0}{\sqrt{1 + \frac{4\omega^2 h_0^2 t}{3\eta}}} \quad (3.3)$$

where η is the solution viscosity, ω the spinning speed, t is the spinning time and h_0 is the starting thickness of the liquid layer. The assumptions required by this equation are rarely satisfied in reality, but it is enough for stating that thickness should decrease with ω and increase with η . There are some issues that need to be accounted for: if the solution is too viscous and/or ω is too low, a ridge may form near the edge of the substrate, leading to a non-uniform thickness. Usually commercial resists come with spinning protocols that reduce this problem. Then, presence of dust or other small particles gives rise to irremovable defects, therefore the surface must be cleaned thoroughly beforehand and the whole process should be conducted in a clean room. Evaporation rate is also relevant and spin coaters usually have a controlled atmosphere.

Spinning is followed by a bake on a hot-plate or in a oven, in order to fully evaporate the solvent and relieve mechanical stresses. When necessary, very detailed programs for spinning speed and temperature are developed in order to reach the best quality and reproducibility.

3.4 Exposure

The exposure process is at the heart of lithography; here the pattern is encoded on the sample in terms of deposited energy. In EBL, an electron beam is scanned on the surface in a serial manner, therefore the time needed for completion scales with area. EBL is slow compared to parallel techniques, such as UV and nano-imprinting lithographies, and it is employed for prototyping or creating UVL masks and nano-imprinting masters. Features of EBL instrument are described in § 3.4.1

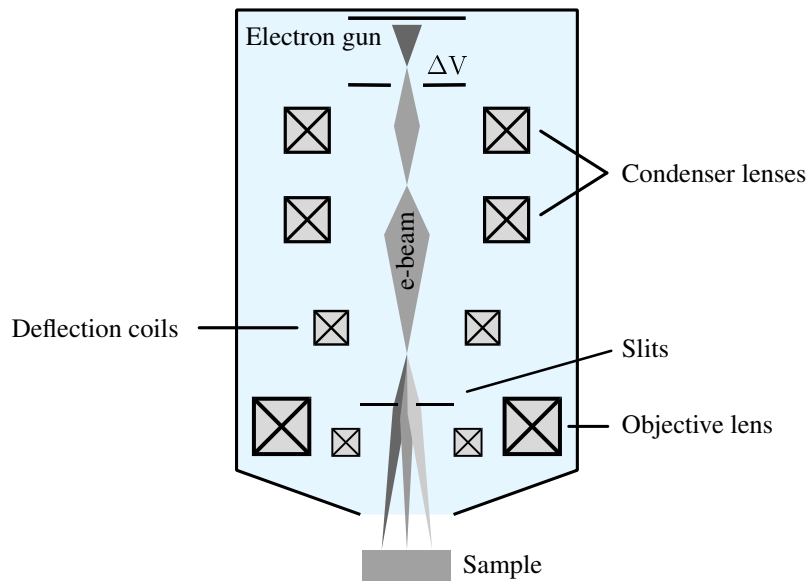


Figure 3.6: Scheme of an electron beam tool. EB lithographers and SEMs share the same architecture, except for SEM detectors.

In § 3.2 the need for tuning dose and accelerating voltage of electrons has already been discussed, but some more adjustments must be applied to the pattern before exposure, in order to counterbalance the so-called proximity effect. The microscopic processes and proximity effect are explained in § 3.4.2.

3.4.1 Electron Beam Lithographer

The scheme of a generic electron beam lithographer is shown in Fig. 3.6. Its components are functionally equal to those of a SEM, in fact many EBL set-ups rely on a modified SEM, and native EBL can perform SEM imaging. Native EBLs show better performances in terms of speed and overall quality of patterns, major differences are:

- Distortions and aberrations are generally higher in SEM, especially near the borders of the image field. Since raster images have no more than 2000 lines, they do not need precision greater than 1 part in 2000. In EBL wider fields are sometimes desired, often they exhibit precisions higher than 1 part in 30 000;
- One field of view may be not enough for nano-fabrication, then stage must be moved as precisely as possible. Movement error, named stitching, could cause structures to be fabricated on dislocated locations. Since in SEM this is not an important issue, as the operator can give constant feedback and correct position, it is sufficient to estimate coordinates from the number of steps actuated by the stepper motor of the stage. EBL doesn't get any human feedback during the process, therefore interferometric measurements must be employed in order to limit stitching to

a few nm over the full run of stage;

- In SEM, images can afford to be taken in ~ 20 seconds, therefore scan coils do not need to be fast and they are built with high inductance; in EBL speed is a limiting factor, the same component is made with multiple shorter and faster coils;
- Currents are generally higher in EBL (nA compared to 10s of pA), these might increase probe size but make exposure faster.
- EBL can reach higher accelerating potentials, which result in higher resolution;

A modified SEM can be good if single small structures are to be built, but the bigger the pattern, the better is to use a native EBL. In this work a modified SEM was used for exposure, fabrication requirements affected the design pattern and therefore it was important to know beforehand its limits in terms of resolution and speed. An analysis on the time taken by an exposure job gives also an insight on how the process works. First, EBL software accepts as input a vectorized image of the pattern, the most common format is gds2, but then it converts it into a set of pixels and of paths connecting them. This process, called fracturing, usually has no impact on overall duration as it is done in parallel with slower processes. Then, pixels are exposed to the electron beam for a certain amount of time, called *dwell* time. Given pixel area A , beam current i and dose to apply D , dwell time is:

$$t = \frac{A \times D}{i}, \quad (3.4)$$

which, multiplied by the total writing area, gives the *beam* time, that is the time spent on actually writing the pattern. Assuming a clearing dose $D_c = 300 \mu\text{C}/\text{cm}^2$ (PMMA), to be applied over 1cm^2 on a pattern with filling factor 0.25 (25% of the total area is to be written) and $i = 2 \text{nA}$, beam time is $t \simeq 40000 \text{s}$. Actually this is a best-case scenario, since steering the beam from pixel to pixel involves some steps: blanking the beam, moving the electromagnets, waiting for their settling and de-blanking the beam. Instruments are characterized by their maximum frequency of steering; this is where faster scan coils make the difference, native EBL exhibit higher working frequencies. If the pattern is big and many field views are required, stage movement may also take its toll. If the pattern is dense, then *stage time* is negligible, but a sparse pattern could require many movements and add up to one hour.

Since the beam is cut in size by slits, current can be modulated through slit aperture: the wider and the higher the current, but also the wider the focused spot on the sample. One should find a compromise between slit aperture and resolution. Another important parameter is the working distance, the distance between the last lens and the sample, which ultimately defines the maximum field size, the area which can be covered by the beam without involving stage movements. This is a very important parameter in modified-SEMs, as it

determines the maximum extent of patterns the instrument is capable to expose without stitching. The higher the working distance and the larger the maximum field size, but at the same time the thicker the focused spot, due to the reduction of numerical aperture. As with slit aperture, a compromise must be found between field size and resolution.

Summarizing, time needed for an exposure job depends much on the instrument and the writing area. Slit aperture and working distance can then be modulated in order to find the best compromise between execution time, maximum field size and resolution.

3.4.2 Electron collisions and proximity effect

The process of beaming high-energy electrons in materials has been studied for a long time because of its applications in lithography, microscopy and characterization techniques. Of our interests are the phenomena that lead to energy transfer from beam to resist material, which locally enhances or decreases the etching rate. We can identify two major phenomena: scattering and generation of secondary electrons.

Scattering involves collision of an high-energy electron with an atomic nucleus, the former gets slowed and steered, the latter acquire some kinetic energy. Both elastic and anelastic collisions occur, but when electrons have sufficiently high energy ($>10\text{KeV}$), the former is dominant and it is commonly called Rutherford scattering. The probability of such collisions is represented by the scattering cross section, which is defined for a solid angle $d\Omega$ (Rutherford model):

$$\frac{d\sigma}{d\Omega} \equiv \frac{\# \text{ of particles scattered into } d\Omega}{\text{incident intensity} \cdot \text{unit time}} = \left(\frac{Z\alpha(\hbar c)}{4E_k \sin^2 \frac{\theta}{2}} \right)^2 \propto Z^2 E_k^{-2} \sin^{-4} \frac{\theta}{2} \quad (3.5)$$

where Z is the atomic number of the encountered ion, $\alpha \simeq 1/137$ is the fine structure constant, $\hbar \simeq 6.63 \times 10^{-34}$ J/s is the reduced Planck constant, c is the speed of light, E_K is the non-relativistic energy of the incoming electron and θ is the scattering angle. Since the resist layer is made of light atoms (H, C, O; low Z) and incoming electrons have an high energy (E_K), only low- θ forward scattering has a decent cross section and the beam retains a narrow width. But most electrons enter into the substrate, where they get slowed (lower E_K) by heavier atoms, so higher back scattering angles are accessible; here the beam widen by micrometers and electrons can eventually re-enter back into the resist and deposit energy at longer distances from the beam centre. Therefore, when aiming the beam to a point on the surface, energy is also deposited nearby according to a cylindrically-symmetric distribution, called Point Spread Function (PSF); this phenomenon is named proximity effect. When a collision occurs with an other electron, the amount of transferred energy is usually sufficient for the second electron to escape its atom's potential, generating a secondary electron and the desired radicals. Multiple

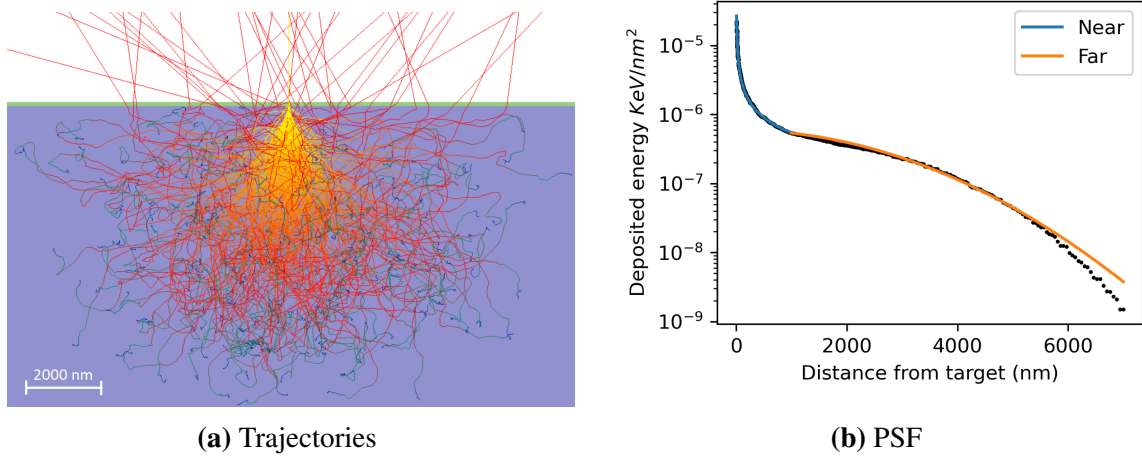


Figure 3.7: Electron trajectories simulated with CASINO3; parameters: 100 nm of PMMA on $10\mu\text{m}$ of silicon, 30 KeV, 10^6 trajectories calculated and 200 shown. Colours of trajectories represent instant energy. From the simulated PSF, it is evident that a simple Gaussian, a parabola on logarithmic scale, is enough for describing the long range (> 1000 nm) energy deposition only. Shorter-distance effects are better described by $E = Cx^{-b}$, $C = 8.7 \cdot 10^{-5}$, $b = 0.736$.

collisions lead to a cascade of electrons, which widen further the PSF.

There are many empirical models describing the PSF, the simplest one considers the sum of two Gaussian distributions^[26]: a narrow one representing the forward scattering contribute, a wider one for back scattered electrons:

$$\text{PSF}(r; \beta_f, \beta_b, \eta) = G(r; \beta_f) + \eta \frac{\beta_f^2}{\beta_b^2} G(r; \beta_b), \quad G(r; \sigma) = \frac{1}{\sqrt{2\pi\sigma^2}} \exp\left(-\frac{r^2}{2\sigma^2}\right) \quad (3.6)$$

where β_b, β_f are the standard deviation of electrons due to substrate back scattering and resist forward scattering, respectively, and η is a parameter that regulates their ratio. Values mainly depend on materials, layer thickness and electron energy; their orders of magnitude are $\beta_b \sim 3\mu\text{m}$, $\beta_f \sim 15\text{nm}$, $\eta \sim 0.5$.

PSF can be calculated through Monte Carlo ray-tracing simulations (Fig. 3.7). In a simulation, many trajectories are created: each trajectory is the sum of paths between collisions, whose length and scattering angle are randomly sampled from theoretical distributions^[11]. Radial distribution of backscattered electrons and their energies are then collected from the trajectories. A free software implementing such algorithm is CASINO3^[5].

In EBL, the target pattern can be seen as a function which takes binary values, $P(\mathbf{r}) : \mathbf{r} \rightarrow [0, 1]$, while the dose (or energy) map to be exposed takes rational values $E(\mathbf{r}) : \mathbf{r} \rightarrow \mathbb{Q}$; the naive approach sets $E(\mathbf{r}) = D_c P(\mathbf{r})$. The actual applied energy $E'(\mathbf{r})$ is the convolution of

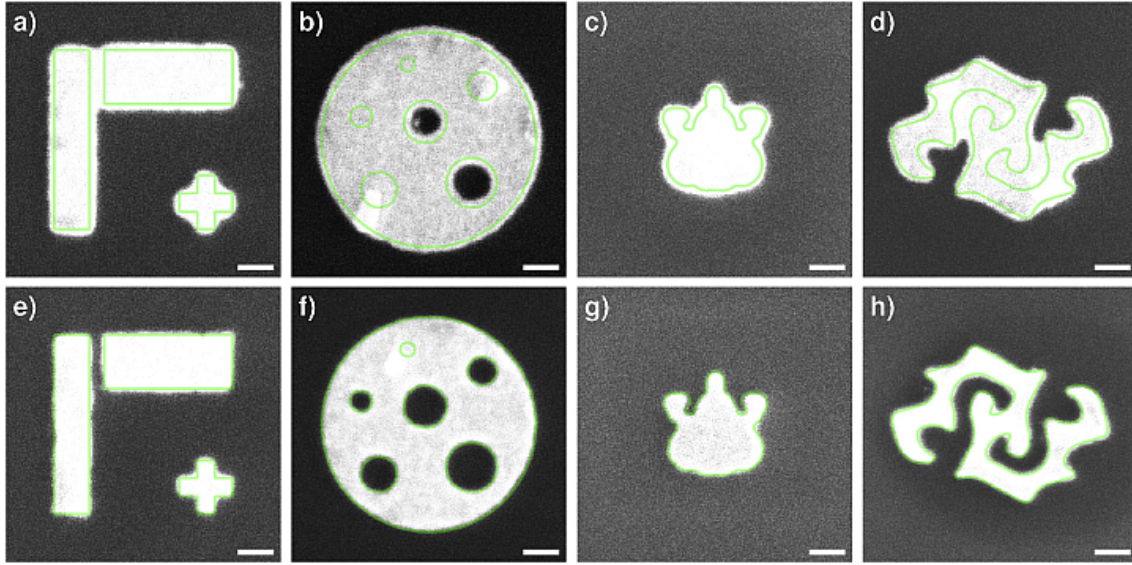


Figure 3.8: Proximity effect in practice: images on the first row clearly show the deformations due to PE (green lines are the target shapes); on the second row a correction has been applied and results closely resemble the target. Scalebar is 100 nm. Reproduced from Eriksen et al.^[14].

$E(\mathbf{r})$ and $\text{PSF}(\mathbf{r}')$:

$$E'(\mathbf{r}) = E(\mathbf{r}) * \text{PSF}(\mathbf{r}') \quad (3.7)$$

Then, when resist is developed, areas with exposure above a threshold value τ are removed (for positive resists), the outcome pattern becomes:

$$P'(\mathbf{r}) = H_{\tau}(E'(\mathbf{r})) \quad H_{\tau}(d) = \frac{1 + \text{sign}(\tau - d)}{2} \quad (3.8)$$

where $H_{\tau}(d)$ approximates the contrast curve on the energy domain. $P'(\mathbf{r})$ is different than $P(\mathbf{r})$, if deformations in the order of ~ 100 nm are relevant to the design, a correction must be applied, as shown in Fig. 3.8.

There are many Proximity Effect Correction (PEC) algorithms^[21], usually they act by modulating doses and/or deforming shapes in $E(\mathbf{r})$. The basic procedure of state-of-the-art algorithms is to deconvolve the target pattern by PSF on the Fourier space^[12]:

$$E(\mathbf{r}) = D_c F^{-1} \left[\frac{F[P(\mathbf{r})]}{F[\text{PSF}(\mathbf{r})]} \right] \quad (3.9)$$

Advances have been made for improving accuracy and performances, by taking into account also the contrast curve and by reducing computational efforts through Fast Multipole Method and numerical optimizations^[14,32].

3.5 Development

After sensitization of resist, development actually creates the pattern on the sample. Wet etching is the technique employed for the task, as it is fast and effective. As explained in § 3.2, the phenomenon involves solubilization of polymer in a solvent. It is true that sensitized regions display enhanced solubility, but also unexposed regions can be eroded too, both because of finite contrast and of proximity effects. Some issues then arise:

- The ratio of etching rates of exposed and unexposed regions limits the maximum aspect ratio of resist structures that can be obtained.
- Etching in thin trenches is often limited by diffusion, at which point higher temperatures and lower viscosities become relevant, increasing the complexity of protocol optimization.
- Timing is crucial for fidelity to the desired pattern. The process should last long enough in order to effectively remove exposed regions, otherwise oversized or blurry features emerge. On the other hand, an excessive development (over-development) shrinks the structures and can eventually erase them.

During development, undercuts and overcuts arise. Since the solvent does not reach the substrate immediately, walls near the substrate undergo etching for a shorter time; an overcut should then be expected from wet etching. However, energy deposition is not uniform and undercuts can be obtained. When using low-energy electrons, $\sim 3\text{KeV}$, the electron beam widens as it propagates in the resist, therefore PSF is larger near the substrate. Similar effects can also be obtained with higher energies, due to the fact that mean energy deposition increases along z , reaching its maximum at $\sim 50\mu\text{m}$ in a silicon substrate. In both cases, the isosurfaces of dose follow an undercut profile; in positive resists, this leads to undercut, while in negative resist, it leads to overcut. Sidewall slope may be tuned through dose: the higher the dose, the smaller are etching time differences between different z , and the more negative is the outcoming slope^[20]. In practice, PMMA exhibits undercut at its clearing dose.

3.6 Hard mask deposition and lift-off

Once the target pattern has been carved in the resist, it has to be transferred to the substrate by means of hard mask deposition and subsequent etching (ICP-RIE). Lift-off technique has been adopted, in which deposition of mask material is performed after patterning and it is followed by removal of resist (Fig. 3.9). After lift-off, the former trenches retain a layer of hard mask, while the substrate is exposed to the air in the regions formerly covered by resist; the whole procedure therefore inverts the tone.

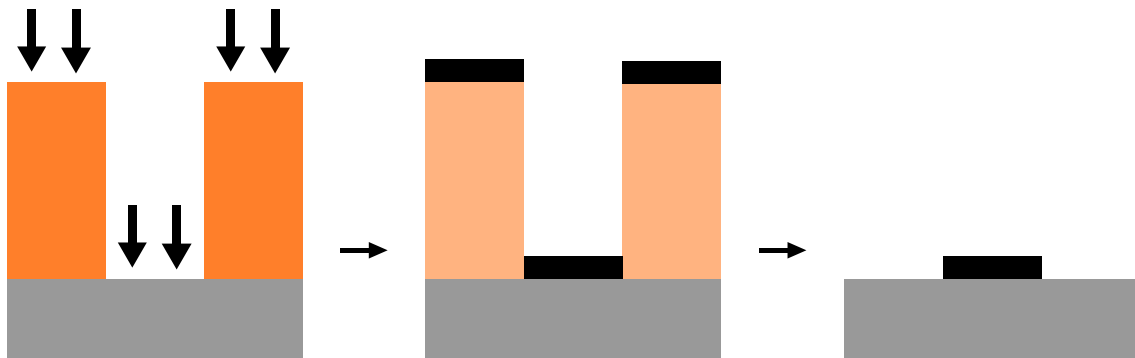


Figure 3.9: Scheme of the deposition/lift-off procedure.

A major issue concerning lift-off is the deposition of some mask material on the walls of resist, which introduces structures that might eventually collapse and degrade the boundaries of shapes. Thinner masks and anisotropic growths reduce the chances of having material on the walls, physical vapour deposition through evaporation can approximate the last requirement. Resist can then be easily removed with acetone.

Height of the mask layer is subject to optimization: it must be high enough in order to undergo ICP-RIE without significant changes in shape and dimensions, while it should be as low as possible in order to deter defects from appearing during lift-off.

The undercut/overcut phenomenon introduced in § 3.2 is very relevant. In the vertical cut case, a perfectly-anisotropic growth is required for zero-coverage of walls. In the overcut scenario, that is not even sufficient to prevent growth on the walls, due to their exposure towards the evaporation target. In the undercut scenario, instead, not only walls are hidden to incoming atoms, but the mask does not even touch them (Fig. 3.10), facilitating a flawless removal of the resist. Therefore the choice of materials and patterning parameters must be such that an undercut is generated, in order to greatly reduce flaws during lift-off. Development may leave residuals on trenches, compromising the hard mask adhesion to the substrate and potentially exposing its underneath. A brief O_2 plasma cleaning should be performed prior to hard mask deposition.

In this work alumina has been used as mask material, instead of the more common chromium, as it shows better performances in ICP-RIE^[18]. Alumina masks in lift-off processes also appear to give better results compared to metal masks: brittle alumina cracks during resist swelling and fragments adhering to the walls gets carried away, leaving less defects on the borders.

3.7 Reactive Ion Etching

Regarding silicon, wet etching has been superseded by dry etching because it is more anisotropic and does not create great amounts of toxic wastes^[23]. Dry etching uses

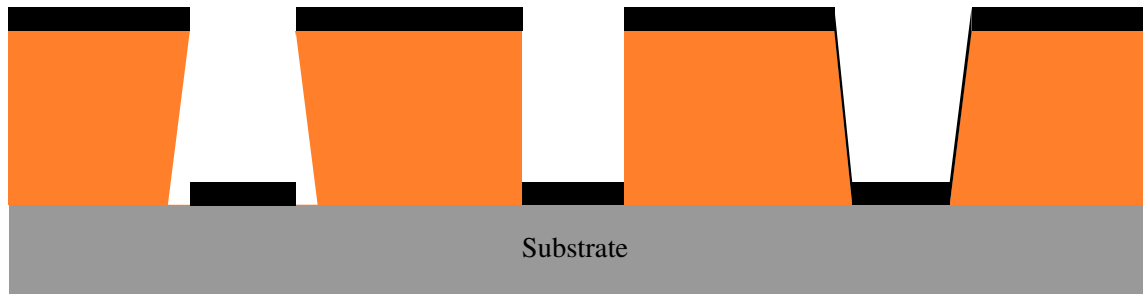


Figure 3.10: Results of a perfectly-anisotropic deposition on different types of cuts.

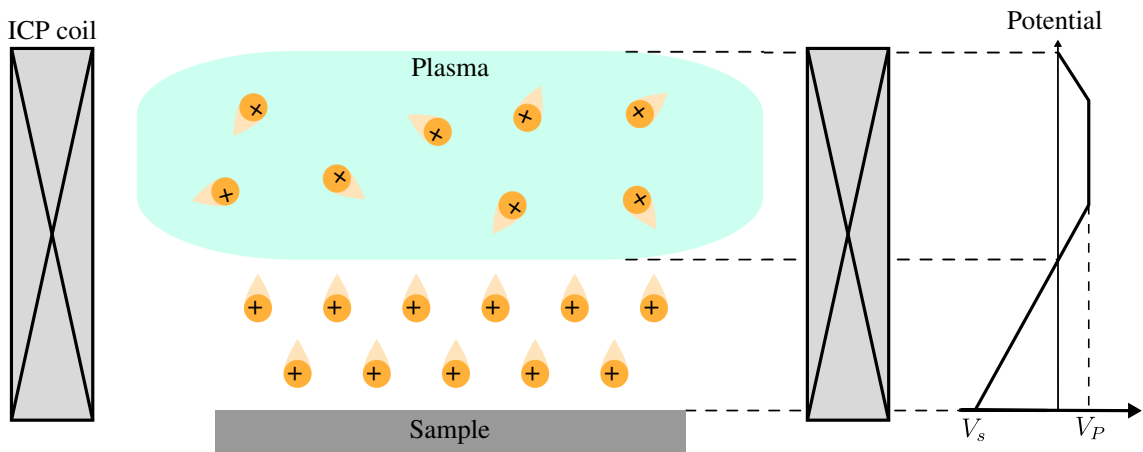


Figure 3.11: Scheme of plasma and ion sheath potential on the sample in ICP-RIE.

plasma to generate high-energy species, ions, radicals and neutral molecules, whose concentrations depend on composition and working conditions of the plasma. The presence of many reactive species makes RIE somewhat difficult to understand completely, as many effects arise from reaction processes and electrostatic interactions.

In this work, RIE was performed with an Inductively Coupled Plasma (ICP). In ICP, instead of planar electrodes, an helical spring is employed. By supplying an alternating electric current to a spring of radius r , an alternating magnetic flux is generated inside:

$$B = \mu_0 n i = \mu_0 n i_0 \cos(\omega t) \quad (3.10)$$

where μ_0 is the magnetic permeability of vacuum, n is the density of wires in the spring, i_0 is the peak current and ω is the alternating frequency. The magnetic flux induces an azimuthal electromotive force:

$$U(r) = -\frac{\partial \int_{\Omega} \mathbf{B} \cdot \hat{\mathbf{N}} dA}{\partial t} = \pi r^2 \mu_0 n i_0 \omega \cos(\omega t), \quad (3.11)$$

which drives electrons to follow closed 8-like trajectories, thus providing plasma generation. ICP, compared to Capacitively Coupled Plasma (CCP), is capable of sustaining higher pressures, leading to faster etchings.

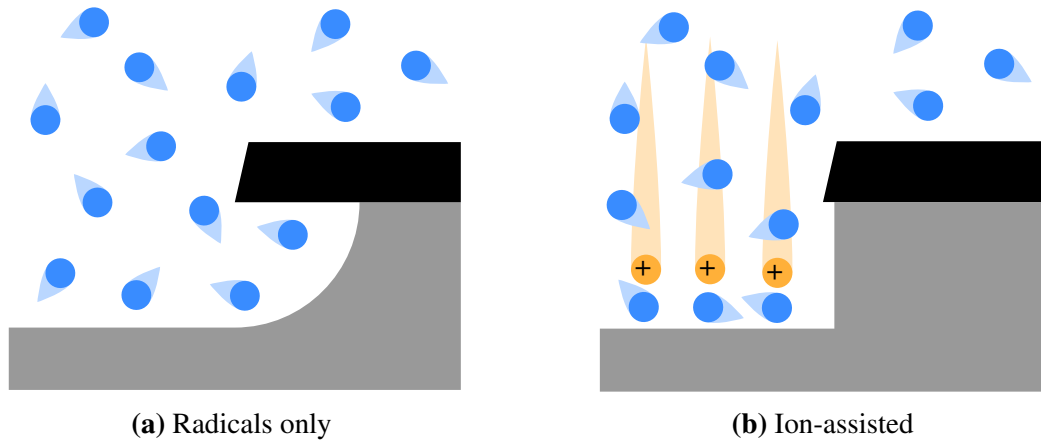


Figure 3.12: Depiction of an isotropic etching given by randomly-directed radicals alone, compared to an anisotropic coupled ion-radical action.

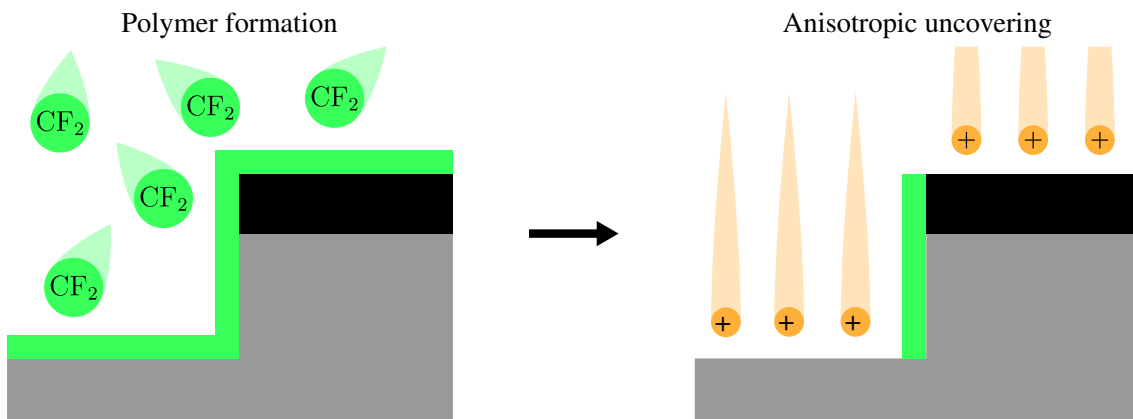


Figure 3.13: Sidewall protection steps during RIE.

Regarding RIE, a plasma with pressure $\sim 10\text{mTorr}$ is induced over the sample with alternating frequency 13.56 MHz . Electrons, being thousands times lighter than ions, move faster and can eventually escape the plasma and negatively charge the bounding surfaces. This phenomenon builds up the so-called *sheath potential*, a negative potential that attracts positive ions, as shown in Fig. 3.11. At the given conditions, the sheath thickness is much shorter than mean free path $d_{sh} \sim 0.3\text{mm} \ll \lambda \sim 5\text{mm}$, causing ions to follow an almost vertical path; therefore, only horizontal surfaces get targeted efficiently, giving a desired anisotropic action. Ion sputtering is not sufficient for efficient etching though, radicals must then be involved in the scheme. In a plasma, a great amount of radicals are generated from reactive species, which can eventually get transported to the surface. Fluorine and chlorine radicals react with silicon and form silicon fluoride and chloride, volatile molecules that can leave the surface (T_{boiling} of SiF_4 is -130°C), thereby removing silicon atoms. Since radicals do not carry charges, they exhibit Brownian motion and taken alone they would perform an isotropic etching, as shown in Fig. 3.12a.

There are two major mechanisms responsible for anisotropic action: ion-assisted etching

and sidewall protection. Coburn et al.^[8] discovered that ions and radicals act synergistically to give enhanced etching. Since ions efficiently hit horizontal surfaces only, the enhanced process is highly anisotropic, as shown in Fig. 3.12b. Enhancement depends both on the material and the gas; on silicon, ion-assisted reaction takes place with Cl^+ and Br^+ species, while the effect is weaker with F^+ ^[25].

When polymer-forming species are added to the plasma mixture, such as fluorinated organic compounds, these can grow a thin uniform polymer layer as shown in Fig. 3.13. Horizontal surfaces, heavily hit by ions, are promptly cleared from the polymer and left exposed to erosion; vertical surfaces, on the other hand, retain the layer and etching is prevented.

Thanks to these phenomena, aspect ratios up to some hundreds can be reached^[18].

An important parameter of RIE is selectivity, that is the ratio between substrate and mask etching rate. When using metal or metal-oxide based masks, metal fluorides may form on the surface, those have low vapour pressure and do not erode much ($T_{\text{boiling}} = 1324^\circ\text{C}$ for AlF_3). Moreover, oxides form strong interactions with protective polymers, as the C-Si bond is weaker than the C-O one, and they have inherently stronger bonds (Bond dissociation energies of diatomic molecules^[17]: Si-Si: 310 KJ/mol; Cr-Cr: 152 KJ/mol; Al-O: 502 KJ/mol). Selectivities up to 68:1 can be obtained with aluminum oxide^[18].

Chapter 4

Fabrication of metalenses

The fabrication processes were executed in the CNR-IOM facilities located at ELETTRA research complexes in Trieste, Italy. Before entering into the details of each technique, some words on the quantities which entangle different steps are needed:

- **Layers' thicknesses** As far as patterning is concerned, resist layer should be as thin as possible. Given a feature size, thinner resists show a lower aspect ratio, which eases the development needs and require lower doses. Lift-off procedure, on the other hand, imposes a lower limit on thickness: it has to be much greater than the mask layer, in order to avoid deposition on the wall, and thicker resist layer shows larger undercuts, further reducing defects that may arise during lift-off. Therefore the need to reduce the minimum mask layer thickness, by employing highly-selective RIE protocols. As mentioned in § 3.6, alumina has been used in this work as mask material, coupled with a $\text{SF}_6/\text{C}_4\text{F}_8$ RIE, it shows selectivities in the order of 70:1^[18]. Given a target trench depth of 850nm, ~ 13 nm of alumina were supposed to be enough, allowing a 100 nm layer of resist to be used. Minimum width of features was also 100 nm, therefore resist structures had ~ 1 aspect ratio. Low enough for PMMA, which should handle at least ~ 4 ^[16,29].
- **Development time and dose optimization** In § 3.5 the influence of development on fidelity was explained. Commercial resists usually come with defined development protocols and tabulated performances: once the maximum aspect ratio is ascertained to be sufficient, only development time must be tuned in order to reach high fidelity. Because of proximity effects, dose also affects the size of features, by expanding or shrinking the domains above D_c . As a matter of fact, the "base" D_c dose is yet to be determined, since PEC only regulates the dose ratios between pixels or shapes ("dose factors") and contrast curve actually depends on development time. Fidelity can then be reached by tuning either development time or dose, let's compare the two approaches. Each would involve writing n patterns, chosen to be

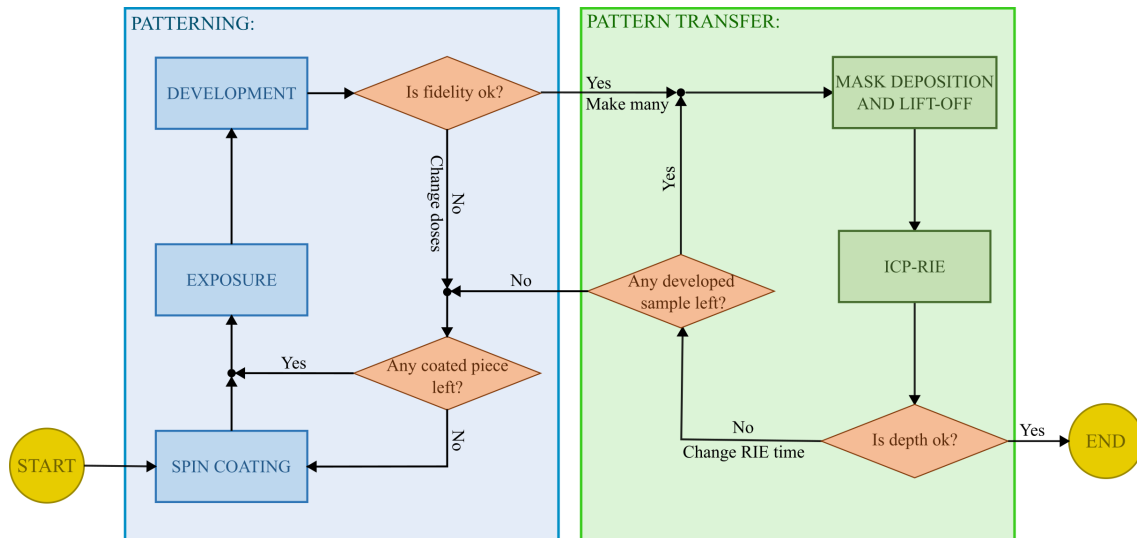


Figure 4.1: Flux diagram of the experimental procedure.

smaller representative of the final one. In order to optimize development, the patterns must be written with same base dose and be sparse enough to be cut in different pieces, then each of them can be developed independently. In dose optimization instead, patterns written with different doses (*dose matrix*) can be closer since a single etch is required. Clearly, the second approach is more efficient materialwise and timewise and it is the one that is usually undertaken. Finally, development time must be fixed to a convenient value: in lab settings, etching is performed manually and we can assume a constant absolute error on time, therefore fast etchings should be avoided because they would suffer from an higher relative error.

- **RIE time optimization** RIE time should be optimized through trial-and-error in order to reach the target depth.

Optimization of doses and RIE time had to be performed in a iterative fashion. Regarding doses, a first mesh of values were chosen, executed and developed; the best values of the first were then selected for generating the second one, and so on and so forth, until satisfying results were reached. From a silicon wafer many pieces could be obtained and from a single exposition many patterns could be written, this degree of parallelization let some shortcuts in the optimization cycles. Finally a flux diagram of the processes could be laid out, shown in Fig. 4.1. Only two parameters are considered in the flux, but quality of the pattern had always to be checked.

4.1 Spin coating

Standard 4-inch silicon wafers were used as substrates (Si-Mat, <100>, n-doped, 1-30 Ωcm). First, the surface had to be deprived of dust and other air-borne nanoparticles,

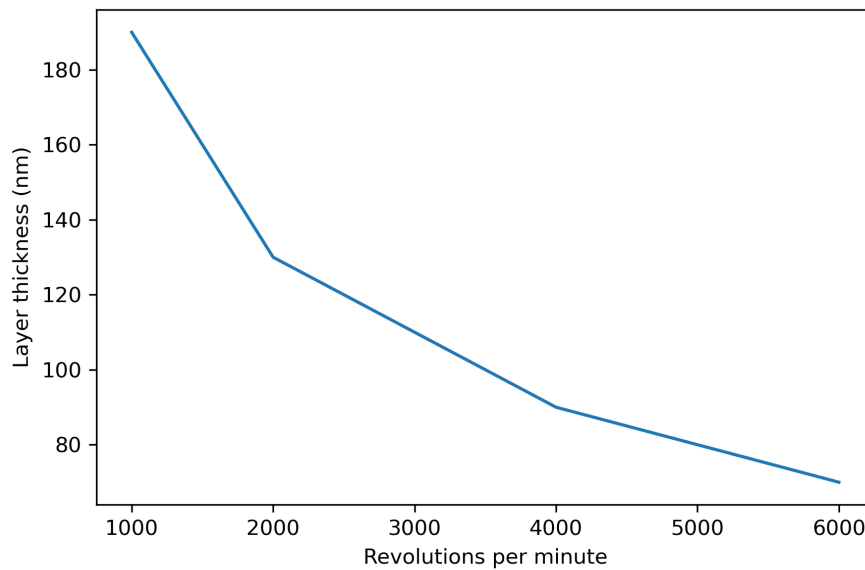


Figure 4.2: Spinning curve of the PMMA used, values have been recovered from its data sheet^[10].

as they would have brought irreversible and significant defects. Therefore the substrate was washed with isopropanol (IPA) while spinning at low speed (~ 500 rpm), dried at 180°C on a hotplate and cooled in air. The whole cleaning and patterning processes were conducted in a ISO 6 clean room.

PMMA (AllResist-P-671.02) was chosen as it is a common positive high-resolution resist. From the tabulated spinning curve (Fig. 4.2), the spin speed required for obtaining a $\sim 100\text{nm}$ layer was estimated to be 3000 rpm. In a spin coater, the cleaned wafer was sprayed upon with a PMMA/chlorobenzene solution until homogeneous coverage, and then spun at 3000 rpm. During the process, colour of the sample changed because of light interference of the solution film; when colour settled, which implied that the film thickness reached a constant value, the sample was slowed down and baked on a hotplate for 5 minutes at 180°C . After cooling, performed naturally in air, the wafer has been cut with a diamond spike and a cutter knife. Coated pieces of size $\sim 1\text{-}2$ cm were so obtained.

4.2 Exposure and development

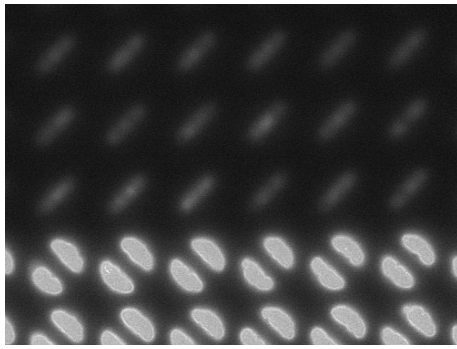
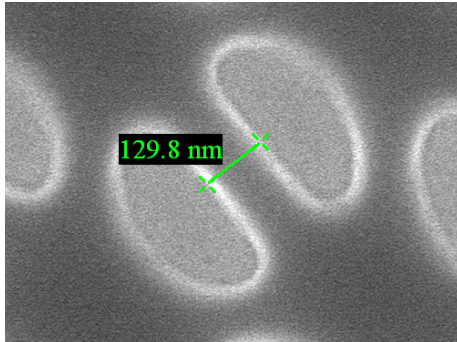
4.2.1 PECless patterns

Before employing a PEC algorithm, some first "PECless" trials had been executed. The EBL system comprised of a Zeiss Sigma 300 SEM actuated by a Raith controller. Being a non-native EBL, each pattern had to fit in a single field view, which could not exceed $\sim 400\mu\text{m}$ due to resolution and finiteness of the depth of focus, which cause aberrations near

the border of wide fields. In Table 4.1, exposure parameters and results of dose matrices are collected. First, smaller patterns were used in order to obtain a faster feedback, wider pattern were used later for a more reliable response. All development processes in this thesis were executed as follows: the sample was immersed in a 1 : 3 methyl isobutyl ketone (MIBK) : isopropanol (IPA) solution for 30 seconds, rinsed with IPA and dried with nitrogen. Metrics used for fidelity evaluation were:

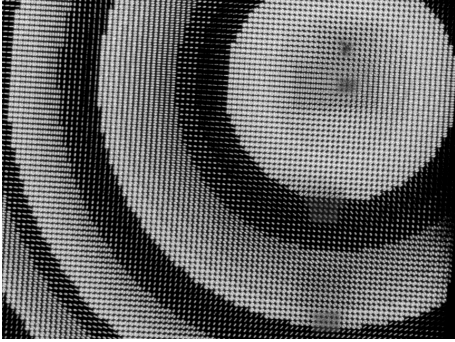
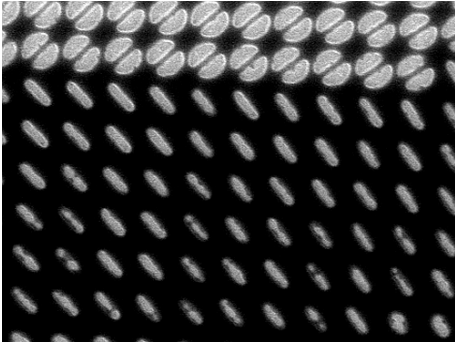
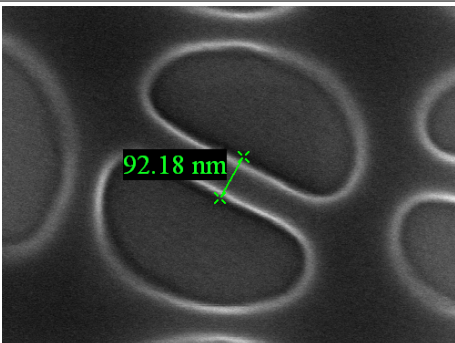
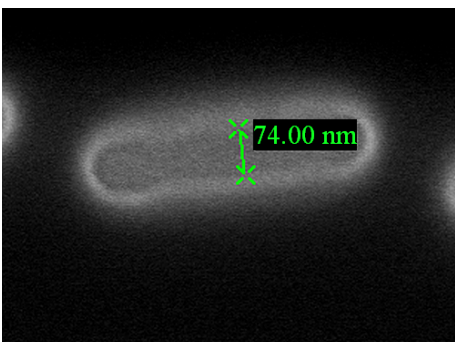
- Shortest dimension of rectangles should have been 100 nm, lower values meant underdevelopment/underdose;
- Distance between features of CB, taken from the centre of the whole pattern, should have been 118 nm (meta-atom 10), lower values meant overdevelopment/overdose;

Table 4.1: Results of exposure and development during dose optimization with a not-PE–corrected design. Note: shapes are valleys.

Exposure data	Dose $\left(\frac{\mu\text{C}}{\text{cm}^2}\right)$	Image	Comment
Matrix 1 Slit aperture: 10 μm , Working distance: 5mm, Field size: 100 μm , Current: 17.5 pA, ΔV : 30 KV	283		CBs are developed, while rectangles are not
			CBs are under-dosed

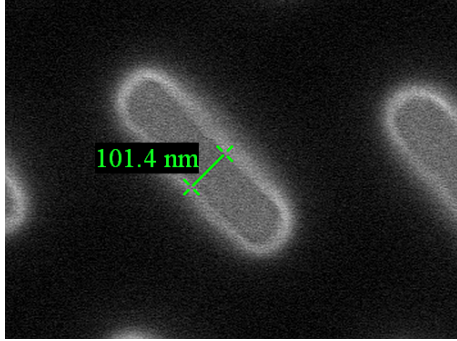
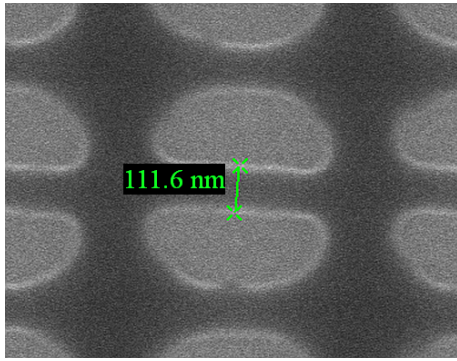
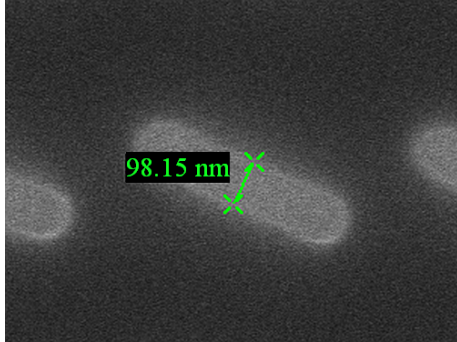
Continued on next page

Table 4.1: Results of exposure and development during dose optimization with a not-PE-corrected design. Note: shapes are valleys. (Continued)

Exposure data	Dose ($\frac{\mu C}{cm^2}$)	Image	Comment
Matrix 2 Slit aperture: 15 μm , WD: 5mm, Field size: 100 μm , Current: 31.4 pA, ΔV : 30 KV	280		CBs are well developed, while rectangles are not
	288		rectangles near CBs ("inner") are more developed than the others ("outer").
Matrix 2 Slit aperture: 15 μm , Working distance: 5mm, Field size: 100 μm , Current: 31.4 pA, ΔV : 30 KV			CBs are overdosed
	303		Outer rectangles are underdosed

Continued on next page

Table 4.1: Results of exposure and development during dose optimization with a not-PE-corrected design. Note: shapes are valleys. (Continued)

Exposure data	Dose $\left(\frac{\mu\text{C}}{\text{cm}^2}\right)$	Image	Comment
			Inner rectangles are well-dosed
Matrix 3 Slit aperture: 15 μm , Working distance: 5mm, Field size: 100 μm , Current: 32.6 pA, ΔV : 30 KV	295		CBs are slightly overdosed
	319		Outer rectangles are well-dosed

The optimal dose for PECless pattern was $\sim 320 \frac{\mu\text{C}}{\text{cm}^2}$ for "outer" rectangles, but it is clear that some areas were well developed while others weren't. In some cases, high fidelity of one region corresponded to erasure of another. The proximity effect was relevant here because rectangular and elliptical meta-atoms have a much lower fill factor than CB ones, low-fill-factor domains were systematically under-exposed while high-fill-factor domains were perfect. Therefore the need for a PEC pattern.

4.2.2 Proximity effect correction

Beamfox^[3] software has been employed for PE correction, it provides built-in PSF calculation and it assigns each structure to one of n dose levels (~ 35 in this case). A detail of the corrected pattern is displayed in Fig. 4.3. A Python script was written to parse the

output of Beamfox into a file readable by the EBL software.

The algorithm behind the software is not disclosed. In order to decouple fabrication protocols from a "black-box" software, a small program has been coded for the same task. Conceptually, PEC is just a deconvolution of the dose image by the PSF, which can be performed in the Fourier space as described in Equation 3.9:

$$I_{\text{out}} = \text{FFT}^{-1} \left[\frac{\text{FFT}[I_{\text{in}}]}{\text{FFT}[\text{PSF}]} \right] \quad (4.1)$$

where I is the digital image of the dose pattern and FFT is the Fast Fourier Transform (FFT), the digital equivalent of the Fourier Transform. But some issues make it hard to implement:

- **Size of the image** In order to well describe the pattern, I should had a pixel for each 10 nm or less. For patterns $\sim 500\mu\text{m}$ wide, that meant images had 2.5 Giga-pixel. Considering a complex double-precision number (16 bytes) for each pixel, this would had required 40 GB of RAM, which a normal personal computer cannot handle. Apart from memory considerations, simple 2D-FFT algorithms are $O(n^2 \log(n))$, where n is the size along one dimension of the image. This scaling makes processing of the whole image inefficient. As described in § 3.4.2, Fast Multipole Method may reduce computational complexity, but it required too much time to learn and implement. Instead, the whole pattern was automatically split in sub-domains, allowing for some padding ($\sim 3\beta_b$) to include inter-domain interactions. Domains would then be processed sequentially.
- **Vector image space precision** EBL instruments accept only a small plethora of file formats and they all represent structures by their boundary points, a sort of vector image. I_{out} and I_{in} , on the other hand, are raster images. First, I_{in} was generated through a rasterisation algorithm, then, I_{out} had to be reduced to a vector image, in which each structure had one dose factor. The latter could have been done in different ways, the algorithm just took for each structure the mean value of its pixels in I_{out} .
- **Algorithm instability** Since $\text{FFT}[\text{PSF}]$ had many points ~ 0 , division by it is unstable. An iterative approach was devised. First, the theoretical dose distribution D_1 was calculated at iteration 1 from I_{in} :

$$D_1 = \text{FFT}^{-1} [\text{FFT}[I_{\text{in}}] \times \text{FFT}[\text{PSF}]] \quad (4.2)$$

In D_1 , underdosed structures had lower doses, while overdosed ones had higher. It was used as a gradient for optimization, after being normalized (mean equal to 0)

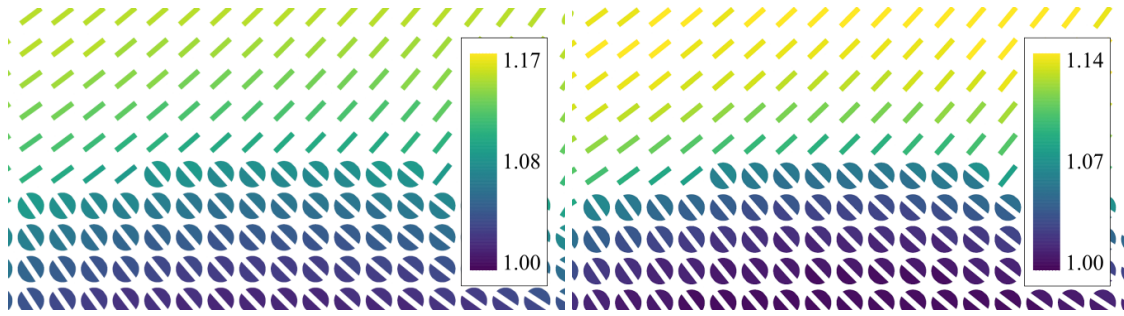


Figure 4.3: Detail of the pattern with corrected dose factors, as calculated by Beamfox and pecrust, respectively. Sparser regions exhibit higher dose factors, results from the two algorithms are very similar.

and multiplied by a step length q :

$$\Delta = -q(D_1 - \text{mean}[D_1]) \quad (4.3)$$

Δ is positive for underdosed structures and negative for overdosed ones. Since each of them had only one dose factor, pixels of a given structure in Δ were equalized to their mean, while pixels not belonging to any were set to 0. The first optimized I_1 was calculated as:

$$I_1 = I_{\text{in}} + \Delta \quad (4.4)$$

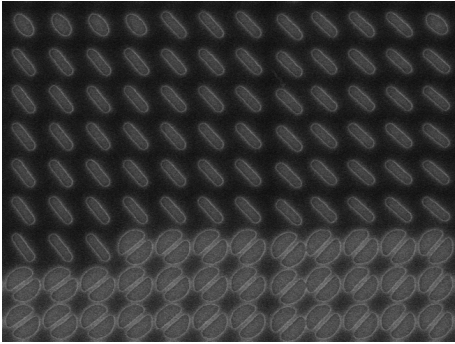
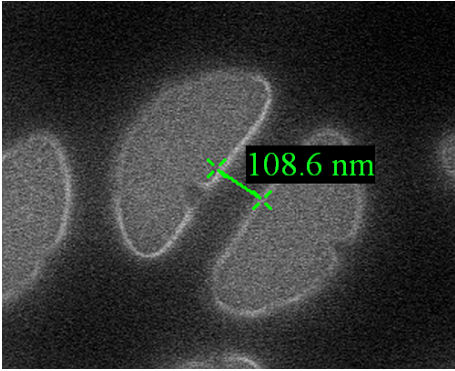
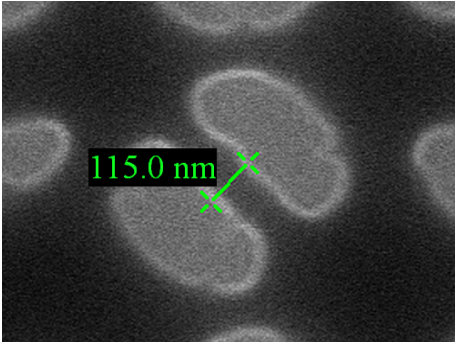
I_1 was used as input for calculating D_2 , and so and so forth for a given number n of iterations. I_n was then taken as I_{out} . The algorithm was empirically verified to be convergent after $n = 3$ iterations.

This algorithm, which we called "pecrust", was benchmarked against Beamfox. Dose factors for metalenses were basically the same for our algorithm and Beamfox. Differences arised for patterns with extreme proximity effects, such as arrays of squares with fill factors ranging from 0.1 to 0.9. We weren't able to try these extreme patterns, anyway our algorithm worked for our purposes.

4.2.3 PEC patterns

Results of PEC-corrected pattern are collected in Table 4.2. Thanks to PEC, both rectangles and CBs are sufficiently well reproduced at approximately $314 \frac{\mu\text{C}}{\text{cm}^2}$ of base dose. Defects shaped as inward-directed spikes of resist emerged in the last samples, probably due to an external electromagnetic interference. These were eliminated by the O_2 plasma cleaning performed prior to hard mask deposition, described in the next section.

Table 4.2: Results from exposure and development during dose optimization with a PEC-corrected design.

Exposure data	Dose ($\frac{\mu C}{cm^2}$)	Image	Comment
Beamfox PEC1 Slit aperture: 10 μm , Working distance: 5mm, Field size: 200 μm , Current: 32.1 pA, ΔV : 30 KV	325		Both CBs and rectangles are overdosed, but seem to share the same effective dose. Spike defects are visible in PEC2 and PEC3
Beamfox PEC2 Slit aperture: 15 μm , Working distance: 5mm, Field size: 400 μm , Current: 30.7 pA, ΔV : 30 KV	317		CBs are slightly overdosed
Beamfox PEC3 Slit aperture: 15 μm , Working distance: 5mm, Field size: 400 μm , Current: 31.5 pA, ΔV : 30 KV	314		CBs are close enough to 118 nm

4.3 Hard mask deposition and lift-off

Prior to hard mask deposition, a brief (5 s) O_2 -plasma cleaning had been performed in order to smoothen resist borders and clean the substrate surface from resist residues and dirt. The ICP-RIE instrument described in § 4.4 has been employed for plasma cleaning. The physical vapour deposition through e-beam evaporation system used for mask deposition is schematically shown in Fig. 4.4. Vacuum was provided by a rotative pump coupled with a cryogenic pump (CTI-Cryogenics Cryo-Torr 8, Edwards Vacuum, working at 26 K), it was measured by a full-range gauge (Pfeiffer Compact). Depositions were performed at $\sim 10^{-6}$ mbar. A electron beam hit the aluminum oxide target, heating it up to high temperature and inducing sublimation. The beam's focus was circularly swept over the target

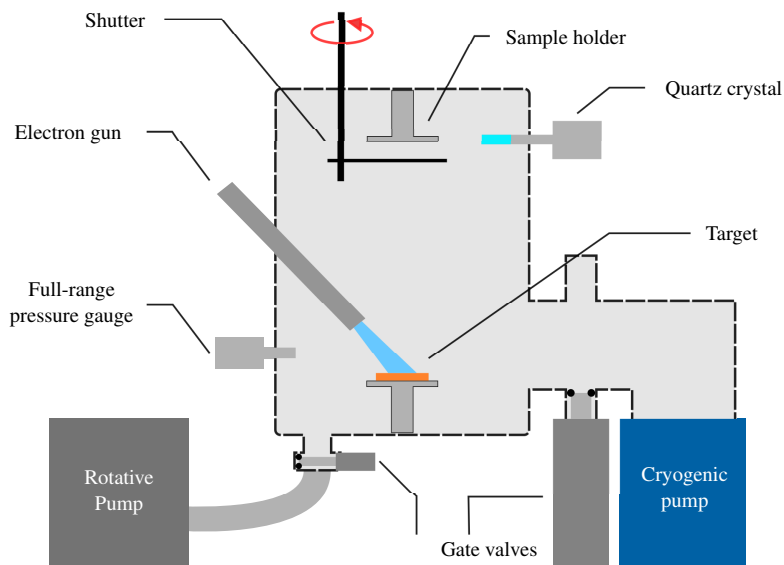


Figure 4.4: Scheme of the system devoted to deposition of hard mask.

in order to evenly distribute heat, rotating frequency was set to 50 Hz and curvature radius was 20% of target size. Progress of deposition was checked through a thickness monitor (Prevac TM 13) relying on a quartz oscillator located near the sample. Addition of material on the oscillator increased its mass, and therefore shifted its resonance frequency. A calibration curve related resonance frequency shift with deposited film's thickness, providing a mean for monitoring deposition progress in real time with $\sim 0.01\text{nm}$ precision, assuming density of alumina remained constant throughout the process. Some deviations may be due to different stoichiometry of alumina, but it was assumed to be negligible. Finally, deposition was controlled by a manual shutter.

Experimentally, the beam was slowly brought to working current (6.5 mA) in order to let heat diffusion homogenize temperature across the target. Once deposition rate, as measured by the quartz oscillator, had stabilized over time ($\sim 0.01\text{nm/s}$), the shutter was opened and measured thickness was zeroed. Upon reaching the desired mask thickness, shutter was closed and the electron beam was slowly attenuated, in order to prevent rapid cooling from compromising the alumina target integrity.

Following deposition, lift-off was executed by immersing the sample in boiling acetone for 15 minutes and subjected to an ultrasonic bath for 1 minute. Afterwards, the sample was washed with RT methanol, acetone contains impurities which might create rings. Finally, a brief check with an optical microscope confirmed the presence of a deposited mask.

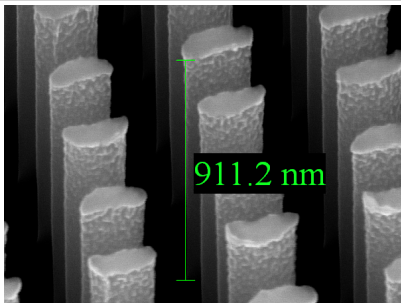
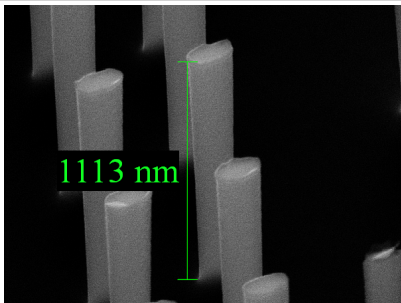
4.4 ICP-RIE

The ICP-RIE system was a STS Multiplex ASE, comprised of a ICP chamber and an antechamber, automated sample and devices management. Process was laid out as following:

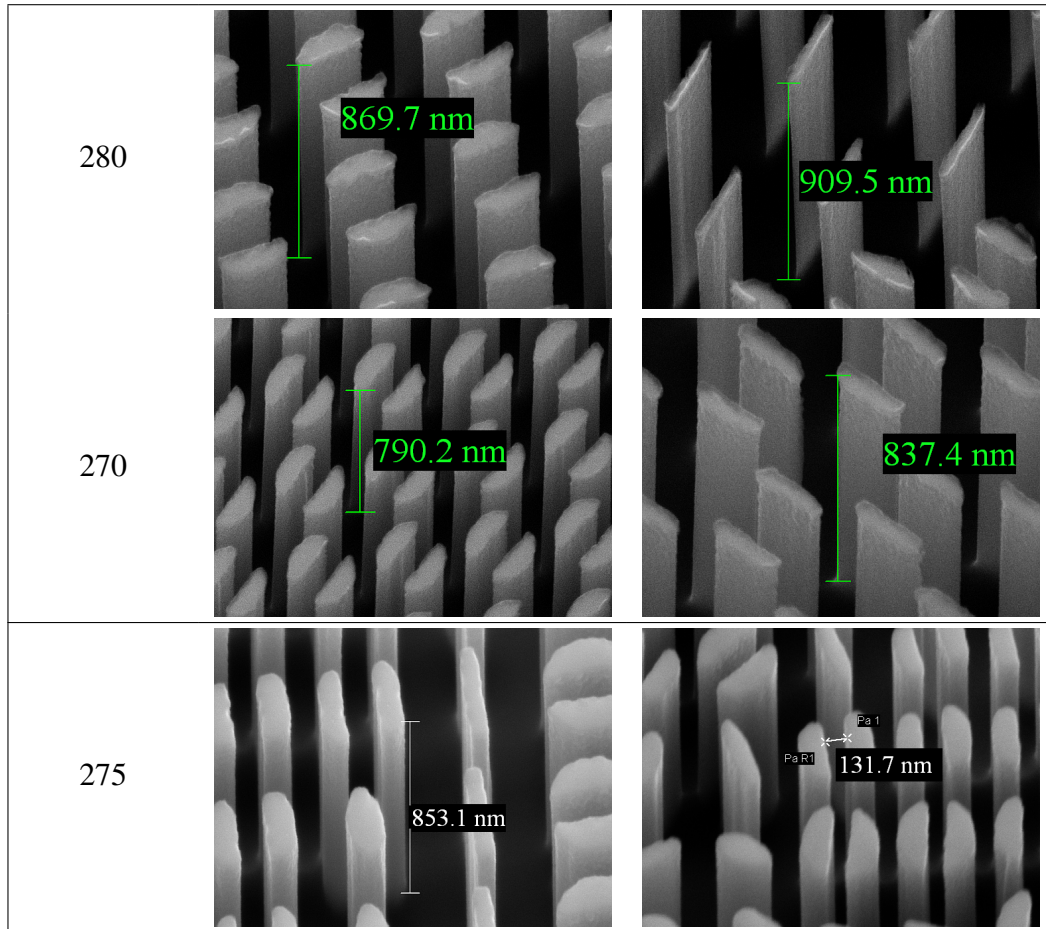
1. Reaching of target pressure 8 mTorr = 10.7 mbar;
2. Surface cleaning by means of a oxygen plasma for 30 seconds;
3. RIE with a 60:30:10 of C_4F_8 : SF_6 :Ar mixture, 100 sccm total flow rate;
4. Post-cleaning for 2 minutes with oxygen plasma, in order to remove polymer residuals and etching by-products.

In the gas mixture, SF_6 acted as a source of F^+ ions, while C_4F_8 was responsible for sidewall protection, as described in § 3.7. Results for different RIE times are shown in Table 4.3. Also in RIE, density of the pattern influenced the process, leading to taller structures in sparser regions. The effect was probably due to faster mass transport in more open areas, which increases etching rate. The best compromise was found between at 275 seconds of processing time. In that case, only one image of a averagely-sparse area (CB-rectangle) has been taken, showing a good match with the required height. Cross-section size was also good, the last image refers to a CB whose distance between its pillars was 130 nm by design. The walls slope was slightly negative, that is, the pillars base is smaller than their upper surface, but in most cases they were almost vertical, so slope should be negligible. Sidewalls sometimes displayed roughness, especially near the metalens surface, probably due to irregularities of the mask borders.

Table 4.3: Resulting pillar's height from different RIE process times and local densities of the pattern.

RIE time (s)	Dense region	Sparse region
300		

Continued on next page

Table 4.3: Resulting pillar's height from different RIE process times and local densities of the pattern. (Continued)

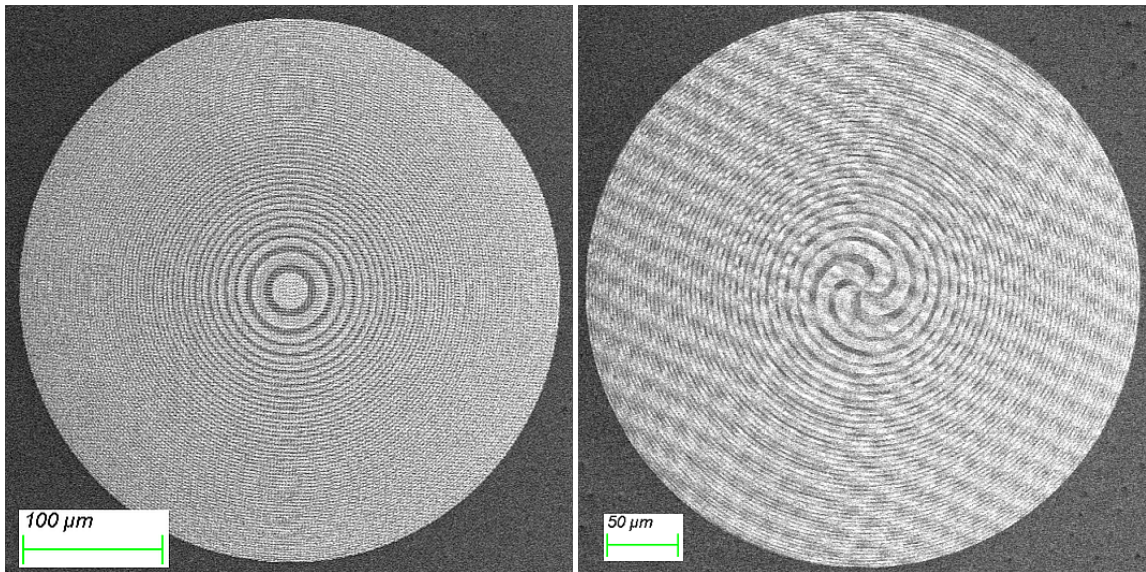
4.5 Summary of processes and parameters

The last images of pillars showed a good fidelity to the designed pattern, therefore optimization of processes and their parameters was considered complete. Table 4.4 summarizes all of them. The resulting metalenses, depicted in Fig. 4.5, were then employed for optical characterization, described in the next chapter.

Table 4.4: Summary of processes and parameters

Parameter	Value
Pre-cleaning: isopropanol, drying through spinning and hot plate heating.	
Spin coating:	
Resist	PMMA AR-P-671.02
Spin speed	3000 rpm
Spin duration	300 s

Continued on next page

Figure 4.5: SEM images of the fabricated ML1 and ML2. An alias effect arose for ML2.**Table 4.4:** Summary of processes and parameters (Continued)

Bake process	Hot-plate
Bake temperature	180 °C
Bake duration	300 s
Exposure:	
D_c	$314 \frac{\mu C}{cm^2} \times \text{PEC dose factors}$
Accelerating potential	30 KV
Working distance	5 mm
Slit aperture	15 μm
Development:	
Solvent	MIBK:IPA - 1:3
Development time	30 s
Rinsing	IPA
O_2 – plasma cleaning:	
Process	ICP-RIE
Plasma pressure	4 mTorr
Cleaning time	5 s

Continued on next page

Table 4.4: Summary of processes and parameters (Continued)

Deposition:		
Process	e-beam evaporation	
Target	Al ₂ O ₃	
Pressure	~ 10 ⁻⁶ mbar	
Mask thickness	14.5 nm	
Etching:		
Process	ICP-RIE	
Etch mixture	C ₄ F ₈ :SF ₆ :Ar - 60:30:10	
Plasma pressure	8 mTorr	
Etch duration	275 s	
Cleanings	Oxygen Plasma	Pre-etch: 30 s, Post-etch: 120 s

Chapter 5

Optical characterization

Optical characterization not only provides data for the actual application of a device, but it is also a functional test validating all the preceding steps of design and fabrication. The first section of the chapter describes the experimental set-up employed for the task, the second section shows and discuss the results.

5.1 Experimental set-up

The optical system should be able to generate a circularly-polarized, monochromatic, tuned at 1310 nm, LG_{00} beam, project it onto the metalens with a beam size no greater than the metalens diameter, and finally obtain a phase and intensity image of the resulting beam. The optical set-up is represented in Fig. 5.1. First, a monochromatic 1310 nm beam was generated by a DFB laser (AeroDiode), collimated by an aspheric lens (A375TM-C, Thorlabs, L_C : $f_C = 7.5\text{mm}$) and horizontally polarized. Then, the beam size has been reduced through a Spatial Light Modulator (SLM, Hamamatsu X13267-08) and a diaphragm located on the Fourier plane of a 4f-telescope (L_3 : $f_3 = 200\text{mm}$ - L_4 : $f_4 = 150\text{mm}$). The SLM applied a phase gradient delay only within a small distance from the optic axis, resulting in a small sized first diffraction order and a large sized zeroth diffraction order. Different diffraction orders are focused in different positions on the Fourier plane of a telescope, the selection of the first order has been accomplished by the diaphragm. Another 4f-telescope (L_1 : $f_1 = 35\text{mm}$ - L_2 : $f_2 = 100\text{mm}$) was put before the SLM, to fit the beam width to the SLM display size and therefore fully exploit the SLM resolution ($12.5\ \mu\text{m}$). Moreover, a beamsplitter was used to separate SLM's impinging and reflected beams, providing also an unaffected beam useful for phase imaging. The "filtering" telescope also further reduced the beam width according to the metalens size, that was $400\ \mu\text{m}$. A quarter wave plate (QWP) was inserted in order to obtain circular polarizations. Then, the metalenses were put in place and a 10x objective made sure that the tightly-focused resulting image could be reasonably enlarged on the camera plane (WiDy

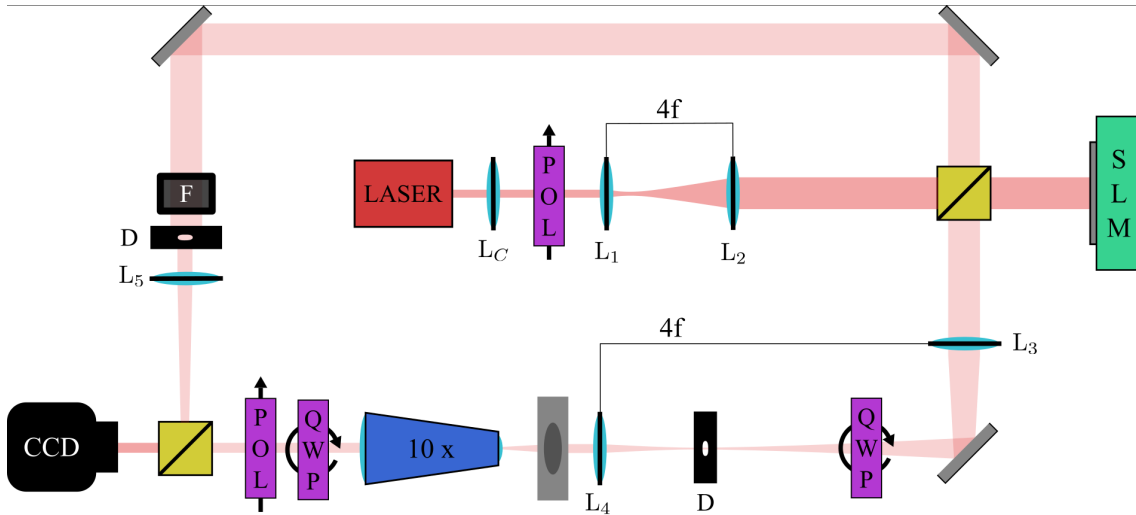


Figure 5.1: Optical bench configuration. Acronyms: POL = Linear Polarizer, L = Lens, SLM = Spatial Light Modulator, QWP = Quarter Wave Plate, D = Diaphragm, 10x = Objective 10x, F = Absorption Filter, CCD = Camera. Yellow boxes are beam splitters, the grey rectangle with a darker ellipse is the metalens, grey rectangles are mirrors.

SWIR 640U-S). A further QWP-polarizer couple was used to filter out zero-order intensity (of the metalens). It would have allowed also for measurement of the zeroth order, but actually it was low that it couldn't be discriminated from noise. Finally, a beamsplitter was inserted to join the resulting and the unaffected beams, allowing them to interfere and get phase images. Size of the unaffected beam was modulated through a lens and a diaphragm, while its intensity was matched with absorptive filters (F). Objective, output QWP-polarizer, camera and output beamsplitter were bonded with a cage structure to ease focusing operations.

5.2 Results

From images of intensity and phase it is possible to characterize the state of the resulting beam. From Fig. 1.1, intensity of $l = 1$ and $l = 3$ should appear as a doughnut, with the latter being wider. The phase recovered from an interferogram should not instead be compared to those of Fig. 1.1b, since slight misalignments between reference and sample beams introduce phase gradients, resulting in a different image. In particular, the superposition of a phase gradient and a phase spiral:

$$U_{l,m} \propto \exp\left(jl\phi + jk'x\right), \quad (5.1)$$

with k' being a parameter depending on the misalignment and x a direction orthogonal to propagation, leads to a so-called fork hologram. Fork holograms for $l = 1$ and $l = 3$ are

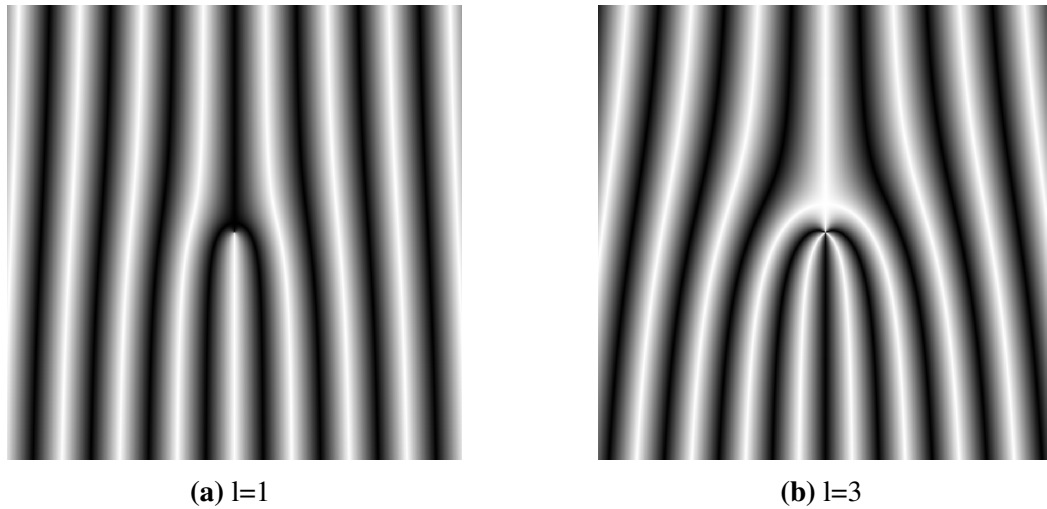


Figure 5.2: Fork holograms for $l = 1$ and $l = 3$.

shown in Fig. 5.2. In general, a central "trunk" gets split in $l + 1$ branches. Holograms for negative values of l are analogous to the positive ones, but mirrored over the line perpendicular to the "trunk" and containing the splitting point.

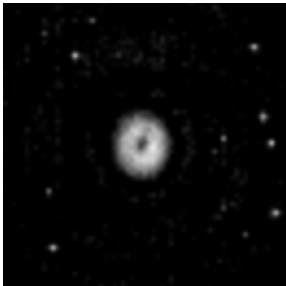
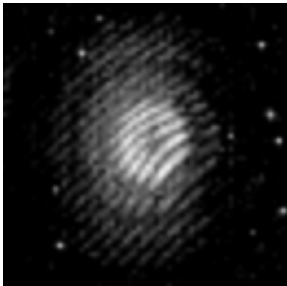
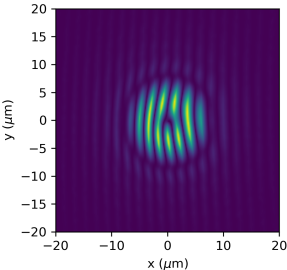
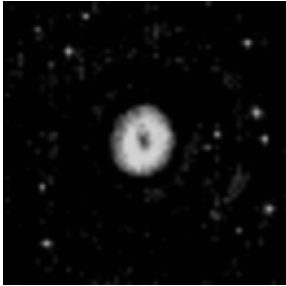
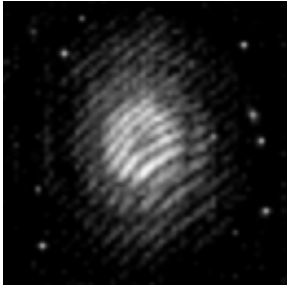
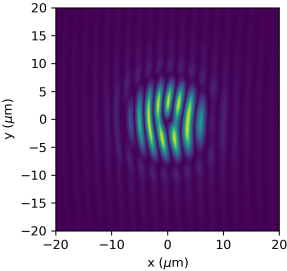

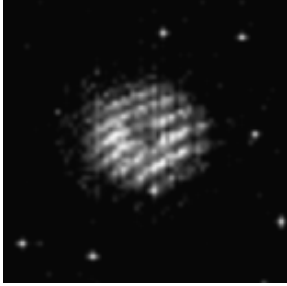
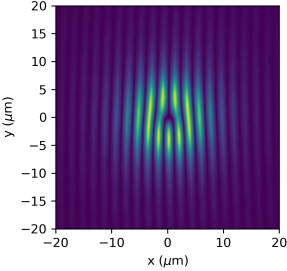

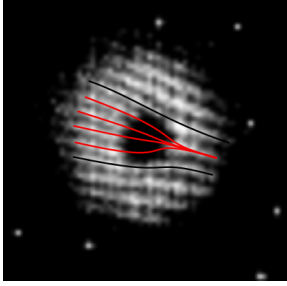
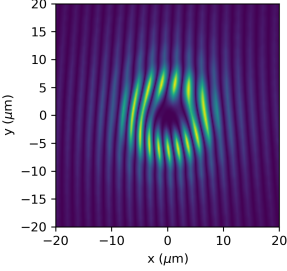
Resulting images and interferograms are displayed in Table 5.1. Interferograms ought to be taken at $500 \mu\text{m}$ from the metalenses, were actually taken slightly out-of-focus ($\sim +20\mu\text{m}$) to increase the size of the spot. Otherwise, interferograms would had been difficult to read. Intensities showed doughnut shapes, the one from LCP configuration of Metalens 2 was larger, suggesting an higher l value. Interferograms confirm the spiral trends of phase. With Metalens 1, a $l = 1$ fork hologram has been obtained for RCP polarization; the hologram inverted when LCP polarization had been selected, confirming that $l_{\text{LCP}} = -l_{\text{RCP}}$. With Metalens 2, again, a $l = 1$ fork hologram has been obtained with RCP polarization. By switching to LCP, the objective had to be shifted $\sim 500\mu\text{m}$ towards the metalens in order to obtain a focused image; as expected, since RCP profile had a designed focal length $500\mu\text{m}$ greater than the LCP one. The interferogram showed a $l = 3$ fork hologram, the centre was dark since the spiral component had much lower intensities due to its large doughnut shape. Simulations, shown in the fourth column of the table, emulated the experimental results with great fidelity. Simulations of ML1 and ML2 LCP were carried out at $d = 520\mu\text{m}$ to include the slight deviation from the focus. Slight deformations in the experimental fork holograms were well reproduced. Deformations could also have been due to small tilts of optical components.

Summarizing, bifunctionality over polarization has been demonstrated at IR frequencies. Despite the challenging high NA (0.38), OAM states were well shaped and zeroth order of the metalens couldn't be distinguished from noise. Design and fabrication protocols were therefore validated by results of optical characterization.

Table 5.1: Resulting images from optical characterization. A resume of metalens properties from § 1.3 helps reminding what we should observe. Some lines have been superimposed on the $l = 3$ interferogram for an easier interpretation. White dots are due to electronic noise. Phases as simulated in § 2.3 were added to a gradient phase and multiplied by the field intensity, leading to the images on the fourth column.

ML1: LCP: $f_{1L} = 500\mu\text{m}$, $l_{1L} = -1$; RCP: $f_{1R} = 500\mu\text{m}$, $l_{1R} = +1$;

ML2: LCP: $f_{2L} = 500\mu\text{m}$, $l_{2L} = +3$; RCP: $f_{2R} = 1000\mu\text{m}$, $l_{2R} = +1$;

Input	Intensity	Interferogram	Simulation
ML1 RCP			
ML1 LCP			
ML2 RCP			
ML2 LCP			

Conclusions

The call for more compact optical devices can be partially answered by bifunctional metalenses, as their independent management of different polarizations makes them able to multiplex multiple devices into one. Their concept is still fairly recent and their implementation is lacking on many areas of optics: not only it involves knowledge about optics, but also different computer simulations and nanofabrication processes^[2]. Every development step imposes requirements on the others, their management thus necessitates a wide scope of competencies.

This thesis aimed to realize the complete development, from the ideas to the actual devices, of bifunctional metalenses working at 1310 nm, one of the two main frequencies adopted in fibre communication.

The proposed metalenses were not designed for a specific practical purpose, but for showing their great flexibility in carrying out rather complex optical operations, in particular the joint high-NA ($NA = 0.38$) generation of OAM beams and focusing. A set of suitable meta-atoms were found through Finite Element Method, it was used then to design the fabrication pattern of metalenses. Resulting discretized phase profiles were validated through Fourier optics simulations. Metalenses were fabricated by means of Electron Beam Lithography, employing the lift-off technique and a ICP-RIE process for transferring the pattern from the resist to the substrate. Finally, optical characterization validated design and fabrication of the devices.

This technology is therefore viable for carrying out complex operations at 1310 nm, practical applications are now free to be explored. Since 1310 nm is a wavelength mainly used in fibre communications, such metalenses might be employed for pushing the frontiers of that field, for example space-division multiplexing^[31] and quantum communication^[27]. In both cases, generation of OAM beams may play a major role, indicating that metalenses similar to those designed in this thesis could be used.

References

- [1] *All About Calma's GDSII Stream Format*. 2022. URL: <https://www.artwork.com/gdsii/gdsii/index.htm>.
- [2] J. P. Balthasar Mueller et al. "Metasurface Polarization Optics: Independent Phase Control of Arbitrary Orthogonal States of Polarization". In: *Phys. Rev. Lett.* 118 (11 2017). DOI: 10.1103/PhysRevLett.118.113901.
- [3] *Beamfox PEC software*. URL: <https://www.beamfox.dk/>.
- [4] J. D. Bull et al. "40-GHz electro-optic polarization modulator for fiber optic communications systems". In: *Proceedings SPIE, Photonics North 2004: Optical Components and Devices 5577* (2004). DOI: 10.1109/comst.2019.2952453.
- [5] *CASINO3: monte Carlo Simulation of electron trajectory in sOlids*. 2016. URL: <https://www.gegi.usherbrooke.ca/casino/>.
- [6] R. Chen et al. "Orbital Angular Momentum Waves: Generation, Detection, and Emerging Applications". In: *IEEE Communications Surveys 22.2* (2020). DOI: 10.1109/comst.2019.2952453.
- [7] S. Chen et al. "Cylindrical vector beam multiplexer/demultiplexer using off-axis polarization control". In: *Light: Science Applications* 10.222 (2021). DOI: 10.1038/s41377-021-00667-7.
- [8] J. W. Coburn and H. F. Winters. "Ion- and electron-assisted gas-surface chemistry—An important effect in plasma etching". In: *Journal of Applied Physics* 50.5 (1979). DOI: 10.1063/1.326355.
- [9] D Cojoc et al. "Laser trapping and micro-manipulation using optical vortices". In: *MICROELECTRONIC ENGINEERING* 78-79 (2005). DOI: 10.1016/j.mee.2004.12.017.
- [10] *Datasheet for PMMA resist 671 series*. URL: <https://www.allresist.com/portfolio-item/e-beam-resist-ar-p-671-series/>.
- [11] H. Demers et al. "Three-dimensional electron microscopy simulation with the CASINO Monte Carlo software". In: *Scanning* 33.3 (). DOI: 10.1002/sca.20262.

- [12] H. Eisenmann, T. Waas, and H. Hartmann. “PROXECCO—Proximity effect correction by convolution”. In: *Journal of Vacuum Science & Technology B: Microelectronics and Nanometer Structures Processing, Measurement, and Phenomena* 11.6 (1993). DOI: 10.1116/1.586594.
- [13] A. G. Emslie, F. T. Bonner, and L. G. Peck. “Flow of a Viscous Liquid on a Rotating Disk”. In: *Journal of Applied Physics* 29 (1958). DOI: 10.1063/1.1723300.
- [14] E. H. Eriksen et al. “Dose regularization via filtering and projection: An open-source code for optimization-based proximity-effect-correction for nanoscale lithography”. In: *Microelectronic Engineering* 199 (2018). DOI: 10.1016/j.mee.2018.07.013.
- [15] *Gds21 Integrated Circuit Layout Parser & Writer*. 2022. URL: <https://crates.io/crates/gds21>.
- [16] S. Gorelick et al. “Direct e-beam writing of high aspect ratio nanostructures in PMMA: A tool for diffractive X-ray optics fabrication”. In: *Microelectronic Engineering* 87.5 (2010). DOI: 10.1016/j.mee.2009.11.091.
- [17] W. M. Haynes. *Handbook of Chemistry and Physics*. 97th ed. CRC Press, 2016. ISBN: 978-1498754286.
- [18] M. D. Henry et al. “Alumina etch masks for fabrication of high-aspect-ratio silicon micropillars and nanopillars”. In: *Nanotechnology* 20.25 (2009). DOI: 10.1088/0957-4484/20/25/255305.
- [19] B. Huang, M. Bates, and X. Zhuang. “Super-Resolution Fluorescence Microscopy”. In: *Annual Review of Biochemistry* 78.1 (2009). DOI: 10.1146/annurev.biochem.77.061906.092014.
- [20] C. Kaspar et al. “Adjustable sidewall slopes by electron-beam exposure layout”. In: *Journal of Vacuum Science & Technology B* 35.6 (2017). DOI: 10.1116/1.4993724.
- [21] P. Li. “A Review of Proximity Effect Correction in Electron-beam Lithography”. In: *Condensed Matter* (2015). DOI: 10.48550/ARXIV.1509.05169.
- [22] Y. Lian et al. “OAM Beams Generation Technology in Optical Fiber: A Review”. In: *IEEE Sensors Journal* 22.5 (2022). DOI: 10.1109/JSEN.2022.3145833.
- [23] T. Lill. *Atomic Layer Processing: Semiconductor Dry Etching Technology*. 1st ed. Wiley-VCH, 2021. ISBN: 978-3-527-34668-4.
- [24] B. A. Miller-Chou and J. L. Koenig. “A review of polymer dissolution”. In: *Progress in Polymer Science* 28.8 (2003). DOI: 10.1016/S0079-6700(03)00045-5.

- [25] K. Nokjiri. *Dry Etching Technology for Semiconductors*. 1st ed. Springer Cham, 2015. ISBN: 978-3-319-10294-8. DOI: 10.1007/978-3-319-10295-5.
- [26] M. Parikh. “Corrections to proximity effects in electron beam lithography. I. Theory”. In: *Journal of Applied Physics* 50.6 (1979). DOI: 10.1063/1.326423.
- [27] X. Ruan et al. “High-Rate Continuous-Variable Quantum Key Distribution with Orbital Angular Momentum Multiplexing”. In: *Entropy* 23.9 (2021). DOI: 10.3390/e23091187.
- [28] *S-Parameter calculation in COMSOL Multiphysics*. URL: https://doc.comsol.com/5.5/doc/com.comsol.help.woptics/woptics_ug_modeling.5.24.html.
- [29] A. Veroli et al. “Dose influence on the PMMA e-resist for the development of high-aspect ratio and reproducible sub-micrometric structures by electron beam lithography”. In: *AIP Conference Proceedings* 1749.1 (2016). DOI: 10.1063/1.4954493.
- [30] A. Vogliardi, F. Romanato, and G. Ruffato. “Design of Dual-Functional Metaoptics for the Spin-Controlled Generation of Orbital Angular Momentum Beams”. In: *Frontiers in Physics* 10 (2022). DOI: 10.3389/fphy.2022.870770.
- [31] A. E. Willner et al. “Orbital angular momentum of light for communications”. In: *Applied Physics Reviews* 8.4 (2021). DOI: 10.1063/5.0054885.
- [32] W. Yao et al. “Efficient Proximity Effect Correction Using Fast Multipole Method with Unequally Spaced Grid for Electron Beam Lithography”. In: *IEEE Transactions on Computer-Aided Design of Integrated Circuits and Systems* (2022). DOI: 10.1109/TCAD.2022.3171441.